23. M. Bose, C. Floss, F. J. Stadermann, R. M. Stroud, A. K. Speck, *Geochim. Cosmochim. Acta* **93**, 77–101 (2012).
24. A. N. Nguyen, L. R. Nittler, F. J. Stadermann, R. M. Stroud, C. M. O. Alexander, *Astrophys. J.* **719**, 166–189 (2010).
25. C. Vollmer, P. Hoppe, F. J. Stadermann, C. Floss, F. E. Brenker, *Geochim. Cosmochim. Acta* **73**, 7127–7149 (2009).
26. C. Floss, F. J. Stadermann, *Meteorit. Planet. Sci.* **47**, 992–1009 (2012).
27. C. Floss, F. Stadermann, *Geochim. Cosmochim. Acta* **73**, 2415–2440 (2009).
28. X. Zhao, C. Floss, Y. Lin, M. Bose, *Astrophys. J.* **769**, 49 (2013).
29. J. K. Hillier *et al.*, *Planet. Space Sci.* **97**, 9–22 (2014).
30. H. Kimura, *Mon. Not. R. Astron. Soc.* **449**, 2250–2258 (2015).
31. J. Slavin, P. Frisch, J. Heerikhuisen, N. Pogorelov, H. R. Mueller, W. T. Reach, G. Zank, A. Li, 38th COSPAR Scientific Assembly, Plenary Meeting (Bremen, Germany, 18 to 25 July 2010), p. 1618.
32. J. D. Slavin *et al.*, *Astrophys. J.* **760**, 46 (2012).
33. V. J. Sterken, P. Strub, H. Krüger, R. von Steiger, P. Frisch, *Astrophys. J.* **812**, 141 (2015).
34. J. D. Slavin, P. C. Frisch, *Astron. Astrophys.* **491**, 53–68 (2008).
35. J. M. Greenberg, J. I. Hage, *Astrophys. J.* **361**, 260 (1990).
36. H. Kimura, I. Mann, E. K. Jessberger, Meteoroids 2001 Conference, B. Warmbein, ed. (2001), vol. 495 of ESA Special Publication, pp. 633–642.
37. P. C. Frisch, J. D. Slavin, *Earth Planets Space* **65**, 175–182 (2013).
38. A. J. Westphal *et al.*, *Meteorit. Planet. Sci.* **49**, 1720–1733 (2014).
39. A. J. Westphal *et al.*, *Science* **345**, 786–791 (2014).
40. J. Leitner, C. Vollmer, P. Hoppe, J. Zipfel, *Astrophys. J.* **745**, 38 (2012).
41. J. P. Bradley *et al.*, *Science* **285**, 1716–1718 (1999).
42. L. P. Keller, S. Messenger, *Geochim. Cosmochim. Acta* **75**, 5336–5365 (2011).

ACKNOWLEDGMENTS

N.A. and F.P. acknowledge European Space Agency faculty funding for travels and meetings that were necessary for the completion of this work. Funding through Deutsche Forschungsgemeinschaft (DFG) within the priority program 1385 "The First 10 Million Years of the Solar System - A Planetary Materials Approach" is acknowledged by K.F., J.B. (grant BL 298/20-2), and R.S., M.T., E.G., J.H., and F.P. (grants TR333/14 and SR77/1). J.H. has received funding from the People Programme (Marie Curie Actions) of the European Union's Seventh Framework Programme FP7 2013 under Reemployment and Eligibility Assessment (REA) grant agreement number 622856. R.S. and F.P. acknowledge funding through Deutsches Zentrum für Luft- und Raumfahrt (DLR), Germany. V.J.S. acknowledges funding through the International Space Science Institute. N.K. acknowledges funding through the DFG. M.T. acknowledges funding by the Klaus Tschira Foundation. We thank J. Leitner, A. Westphal, R. Stroud, L. Nittler, P. Hoppe, H. Ishii, and H.-P. Gail for helpful discussions. We thank three anonymous reviewers for their thorough review of this paper. All CDA data used for this analysis are archived on the Small Bodies Node of the Planetary Data System (PDS-SBN), at http://sbn.psi.edu/archive/cocda.

SUPPLEMENTARY MATERIALS

www.sciencemag.org/content/352/6283/312/suppl/DC1
Materials and Methods
Figs. S1 to S6
Table S1
References (*43*–*61*)

3 June 2015; accepted 3 March 2016
10.1126/science.aac6397

REPORTS

MOLECULAR MAGNETISM

Magnetic remanence in single atoms

F. Donati,[1] S. Rusponi,[1] S. Stepanow,[2] C. Wäckerlin,[1] A. Singha,[1] L. Persichetti,[2] R. Baltic,[1] K. Diller,[1] F. Patthey,[1] E. Fernandes,[1] J. Dreiser,[1,3] Ž. Šljivančanin,[4,5] K. Kummer,[6] C. Nistor,[2] P. Gambardella,[2]* H. Brune[1]*

A permanent magnet retains a substantial fraction of its saturation magnetization in the absence of an external magnetic field. Realizing magnetic remanence in a single atom allows for storing and processing information in the smallest unit of matter. We show that individual holmium (Ho) atoms adsorbed on ultrathin MgO(100) layers on Ag(100) exhibit magnetic remanence up to a temperature of 30 kelvin and a relaxation time of 1500 seconds at 10 kelvin. This extraordinary stability is achieved by the realization of a symmetry-protected magnetic ground state and by decoupling the Ho spin from the underlying metal by a tunnel barrier.

The search for the ultimate size limit of magnetic information storage, and the aim of exploring magnetic quantum properties for information processing, have driven fundamental research toward atomic-scale structures that contain fewer and fewer atoms. Benchmarks for such systems are long magnetic relaxation times, i.e., magnetic quantum states that are stable on the time scales required for storage or quantum computation. Single-molecule magnets (*1*–*6*) are promising candidates as they are chemically robust in ambient conditions and exhibit magnetic bistability at cryogenic temperatures, with a record relaxation time of 100 s at 13.9 K for N_2^{3-} radical-bridged dilanthanide complexes in the bulk phase (*6*). Further reducing the number of constituent atoms in such systems, however, implies removing the organic ligands, thereby bringing the magnetic core in direct contact with a surface. Presently, the smallest magnets are antiferromagnetic Fe_{12} double chains (*7*) and ferromagnetic Fe_5 clusters (*8*) supported on nonmagnetic surfaces. Both exhibit lifetimes of hours below 0.5 K, while supported nanostructures of smaller size retain their magnetic orientation only on a time scale of seconds (*9*, *10*).

Ultimately, the smallest size of a magnet can be reached with a single surface-adsorbed atom. The magnetism of single atoms has become the subject of intense research (*11*–*17*) since the discovery of a giant magnetic anisotropy for Co atoms adsorbed onto a Pt(111) surface (*18*). However, despite the high magnetic anisotropy originating from the extremely low coordination, all adatom-surface combinations investigated so far are paramagnetic down to 0.3 K, with the longest achieved magnetic lifetime being 230 μs at 0.6 K (*16*, *17*). Thus, in addition to anisotropy, the magnetic states of a quantum magnet need to be protected from quantum tunneling of the magnetization as well as from scattering with electrons and phonons of the substrate. The first condition requires a degenerate ground state doublet with a projected total angular momentum J_z that is protected from mixing with other states by the symmetry of the adsorption sites' ligand field (*19*, *20*). The second requires decoupling the magnetic atom from the phonon and conduction electron baths.

Here, we investigated ensembles of rare-earth atoms, whose spin and orbital moments originate from the strongly localized 4f orbitals and interact weakly with the surrounding environment. Additional decoupling is ensured by choosing an insulating substrate with low phonon density of states, such as MgO. We found that Ho atoms deposited on MgO(100) thin films grown on a Ag(100) surface formed single-atom magnets with a relaxation time that depended on the MgO thickness. Not only did the Ho atoms show magnetic bistability, they also had exceptionally large coercive field and showed magnetic hysteresis up to 30 K, a temperature substantially higher than the blocking temperature of single-molecule magnets on comparable time scales. These exceptional properties originate from a combination of factors—namely, the specific mixing of odd J_z states of Ho in the C_{4v} symmetric ligand field of MgO(100), which protects the magnetization from reversal by tunneling and first-order electron scattering at zero and finite fields, and the weak coupling to the electronic and vibrational degrees of freedom of the substrate, provided by the stiff and insulating MgO buffer layer.

We created a quasi-monodisperse ensemble of individual Ho atoms adsorbed on ultrathin MgO(100) films grown on Ag(100) by depositing minute amounts of Ho at a sample temperature below 10 K, which ensured that the thermal mobility of the adatoms was blocked. Low-temperature scanning tunneling microscopy (STM) images

[1]Institute of Physics, Ecole Polytechnique Fédérale de Lausanne (EPFL), Station 3, CH-1015 Lausanne, Switzerland. [2]Department of Materials, ETH Zürich, Hönggerbergring 64, CH-8093 Zürich, Switzerland. [3]Swiss Light Source, Paul Scherrer Institute, CH-5232 Villigen PSI, Switzerland. [4]Vinča Institute of Nuclear Sciences (020), Post Office Box 522, 11001 Belgrade, Serbia. [5]Texas A&M University at Qatar, Doha, Qatar. [6]European Synchrotron Radiation Facility (ESRF), F-38043 Grenoble, France.
***Corresponding author. E-mail: pietro.gambardella@mat.ethz.ch (P.G.); harald.brune@epfl.ch (H.B.)**

displayed the Ho atoms as localized protrusions with identical apparent heights and widths (Fig. 1A). Ab initio calculations using density functional theory (DFT) in the GGA+U approximation (*21*) identify the O-top as the most favorable adsorption site (Fig. 1B and table S3). Atomic-resolution images of samples with coadsorbed Co or Fe atoms confirmed this assignment (fig. S2). The adatoms were immobile up to 50 K and, therefore, at all temperatures where we characterized their magnetic properties.

X-ray absorption and magnetic circular dichroism spectra (XAS and XMCD) taken at the Ho $M_{4,5}$ edges (3d→4f transitions) with the x-ray beam and magnetic field parallel to the surface normal revealed a pronounced dichroism (Fig. 1D). This magnetic signal indicates the presence of a large localized magnetic moment that aligns along the field direction. Recording the maximum of the XMCD peak as a function of the external field allowed us to measure the magnetization loop of the Ho adatoms. At 6.5 K, we observed a clear hysteresis opening along the out-of-plane direction and a remanent magnetization of 25% of saturation (Fig. 1E). After saturation, the Ho atoms retained their magnetization even in the absence of an external field. In addition, the loop showed a coercive field of 1 T and remains open up to the maximum available field of 8.5 T, indicating a long relaxation time even at extremely high magnetic fields.

This exceptional magnetic stability is related to the symmetry of the Ho quantum states. We identify them by comparing experimental spectra and magnetization curves with multiplet calculations (fig. S6). At zero field, the ground state is a perfectly degenerate doublet. The two states, labeled as $|0\rangle$ and $|1\rangle$, exhibited out-of-plane projections of the total moment $\langle J_z = \pm 4.66 \rangle$ (Fig. 1C). This value matches well with the result of the sum rules directly applied to the experimental XAS and XMCD spectra (*22*). In the C_{4v} symmetry of the O adsorption site, this ground state doublet is a superposition of the the quantum states $J_z = \pm 7; \pm 3; \mp 1$; and ∓ 5, with the first two contributing the most (table S2). Thus, it is protected from first-order spin excitations ($\Delta m = 0, \pm 1$) at any external magnetic field (*20*), which prevents magnetization reversal by electron scattering. In addition, the very low density of vibrational modes in the MgO layer (fig. S9) strongly suppresses first-order scattering with phonons ($\Delta m = \pm 1, \pm 2$). The absence of Ho-MgO vibrational modes in the region of hyperfine level crossing can further slow down relaxation at low fields, as observed for $TbPc_2$ molecules grafted on suspended nanotubes (*23*). Thus, the combination of magnetic ground state, symmetry of the adsorption site, and decoupling from the metal substrate guarantees protection against all first-order scattering and ultimately allows for long magnetic lifetimes.

The first excited state $|2\rangle$ is a $\langle J_z = 0 \rangle$ singlet lying 4.5 meV above the ground state. This energy separation is sufficient to prevent electronic level crossings up to more than 10 T (Fig. 1C), hence the absence of quantum tunneling steps in the hysteresis loop (*3*). Further excited states lie at a higher energy and played no role at the temperatures and magnetic fields used here.

To access the magnetic lifetime, we first initialized the ensemble of Ho atoms in the $|0\rangle$ state by applying an external field B = +6.8 T until saturation was reached. We then swept the magnetic field to near zero (B = 0.01 T) and recorded the time needed for the magnetization of the ensemble to vanish—namely, to reach equal occupation of the $|0\rangle$ and $|1\rangle$ states (Fig. 2A). At a temperature of 10 K, we found an exponential decrease in the XMCD signal with a characteristic lifetime of τ = 1586 ± 131 s (Fig. 2C). Notably, we observed comparable magnetic lifetimes down to 2.5 K (fig. S4A), implying that below 10 K, the magnetic relaxation is essentially driven by nonthermal processes.

Measurements at different photon fluxes revealed that the lifetime of Ho atoms is mostly limited by the secondary electron cascade generated by the absorbed photons. The scattering with these hot electrons reduces the magnetic lifetime, as recently reported for endofullerene single-molecule magnets (*24*). The measured lifetimes hence represent a lower bound to the intrinsic magnetic lifetimes. Extrapolation to the zero-flux limit suggests intrinsic lifetimes of the order of 1 hour at 2.5 K (fig. S4B). Increasing the temperature to 20 K activates thermal relaxation processes and results in a slightly decreased magnetic lifetime of 675 ± 77 s (Fig. 2C). The lifetime of the Ho atoms on MgO is much longer than for Ho

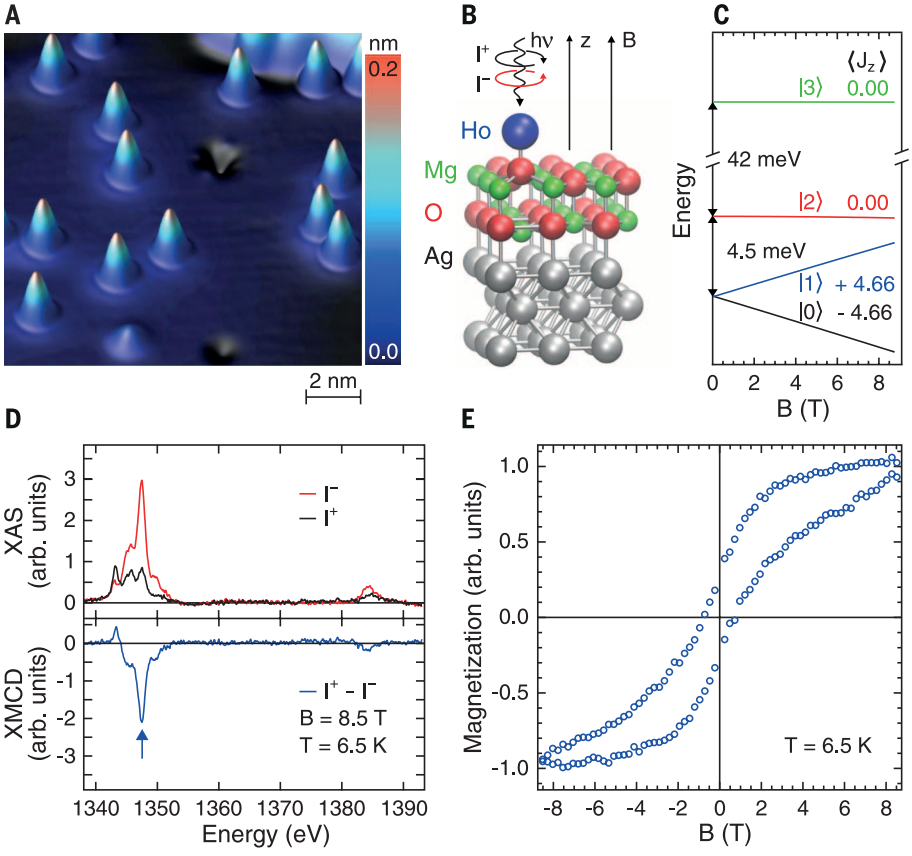

Fig. 1. Ho atoms on MgO films. (**A**) Constant-current STM image of Ho atoms on 2 monolayer (ML) MgO/Ag(100) (tunnel voltage V_t = 100 mV, tunnel current I_t = 20 pA, T = 4.7 K, Ho coverage Θ_{Ho} = 0.005 ± 0.001 ML). (**B**) Adsorption geometry of Ho atoms on top of O on 2-ML MgO/Ag(100) as simulated with DFT, together with a schematic of the XAS experiment. (**C**) Splitting of the lowest quantum levels of Ho atoms from multiplet calculations. Zero-field values of $\langle J_z \rangle$ are reported. (**D**) XAS and XMCD at the $M_{4,5}$ edges for an ensemble of individual Ho adatoms. The arrow points to the maximum of the XMCD signal that is recorded as a function of magnetic field to obtain the magnetization curves shown in (**E**) (field sweep rate dB/dt) = 8 mT/s, photon flux $\phi = 1 \times 10^{-2}$ nm^{-2} s^{-1}, T = 6.5 K, Θ_{Ho} = 0.01 ML, MgO coverage Θ_{MgO} = 7.0 ML).

ions in $HoPc_2$ (*25*) and Ho-doped bulk crystals (*26*), possibly because of the larger level splitting and the smaller number of vibration modes allowed for atoms adsorbed on surfaces.

We further characterized the magnetic lifetime at a large magnetic field. We prepared the ensemble in the $|1\rangle$ state at $B = -6.8$ T and measured the time needed to fully reverse to the $|0\rangle$ state at $B = +6.8$ T and $T = 10$ K (Fig. 2B). We observed an exponential increase in the magnetization up to saturation with $\tau_{rev} = 1223 \pm 69$ s (Fig. 2D). Thus, the Ho atoms on MgO retained their long lifetimes even at a very high field where single-molecule magnets typically exhibit faster relaxations because of level crossing, quantum tunneling of the magnetization, or scattering with phonons (*1*–*5*).

To probe the temperature dependence of the remanence and of the coercive field of Ho atoms, we recorded hysteresis loops in the most favorable experimental conditions, i.e., using the fastest field sweep rate *dB/dt* and lowest photon flux achievable (Fig. 3A). Under these conditions, the hysteresis opening at 10 K (Fig. 3B) was even wider than the one in Fig. 1E, showing a coercive field of 3.7 ± 0.3 T and a remanent magnetization of 50% of saturation. In addition, the hysteresis remained open up to 30 K, and only at 40 K was the magnetization loop essentially closed (Fig. 3C). These results further show that the magnetic quantum states of Ho atoms were notably protected against scattering with Ag conduction electrons and MgO phonons.

Although the Ho ground state was protected against magnetization reversal via first-order electron-spin excitations, it is possible, in principle, to reverse the magnetization via direct scattering with phonons or by two-electron or -phonon transitions through the first excited state. The reversal processes that are triggered by the scattering with conduction electrons and with the soft phonon modes of the underlying metal are expected to critically depend on the thickness of the MgO layer. Accordingly, we observed that the hysteresis loops of Ho atoms became narrower when the thickness of

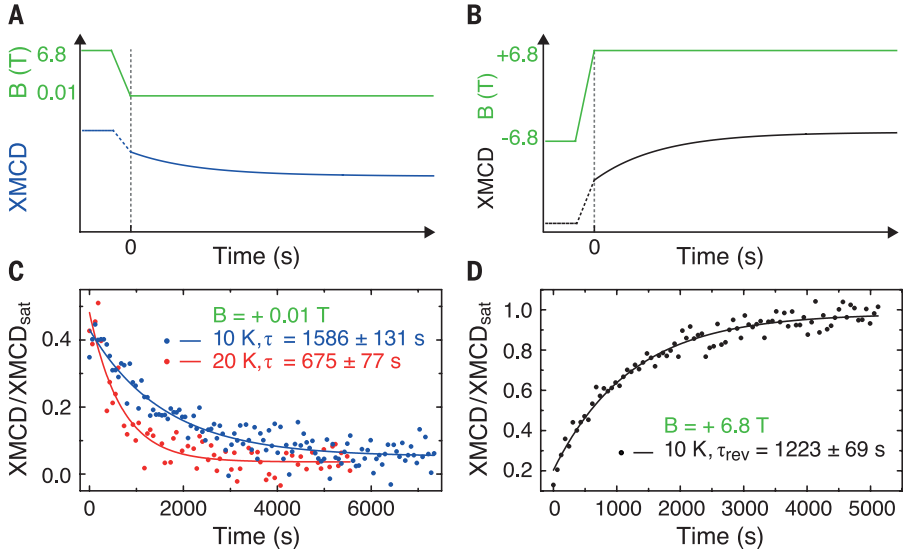

Fig. 2. Magnetization lifetime. (**A** and **B**) Scheme of the measurements. After saturation at $|B_{max}| = 6.8$T, the field was swept to the indicated values. Measurements of XMCD started at the end of the sweep. (**C** and **D**) Time evolution of the maximum XMCD intensity (dots) normalized to the saturation value at $B = +6.8$ T ($\Theta_{Ho} = 0.015$ ML, $\Theta_{MgO} = 6.0$ ML, $\phi = 0.14 \times 10^{-2}$ nm^{-2} s^{-1}, *dB/dt* = 33 mT/s). Exponential fits (solid lines) give the magnetic lifetime τ and reversal time τ_{rev} of the Ho atoms.

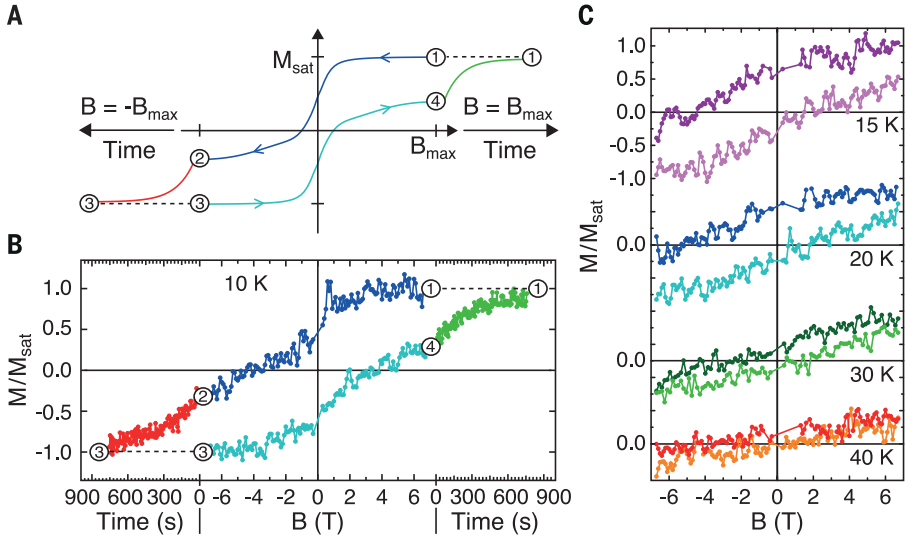

Fig. 3. Magnetic hysteresis at increasing temperatures. (**A**) Scheme for the hysteresis measurements at a fast sweep rate of the magnetic field. We first kept the magnetic field at $+B_{max}$ for sufficient time to reach $+M_{sat}$ (*1*), then measured *M* while sweeping the field to $-B_{max}$ (*2*). This fast sweep leaves the system out of equilibrium at B_{max}. Thus, we allow the system to relax at constant $B = -B_{max}$ until equilibrium is reached (*3*) before starting the new branch of the loop (3-4-1). (**B**) Hysteresis loop recorded at $T = 10$ K following the scheme described in (A). (**C**) Evolution of the hysteresis loop with the temperature (dark, downsweep; light, upsweep). The relaxation part is not shown ($\Theta_{Ho} = 0.01$ ML, $\Theta_{MgO} = 4.3$ ML, $\phi = 0.55 \times 10^{-2}$ nm^{-2} s^{-1}, *dB/dt* = 33 mT/s).

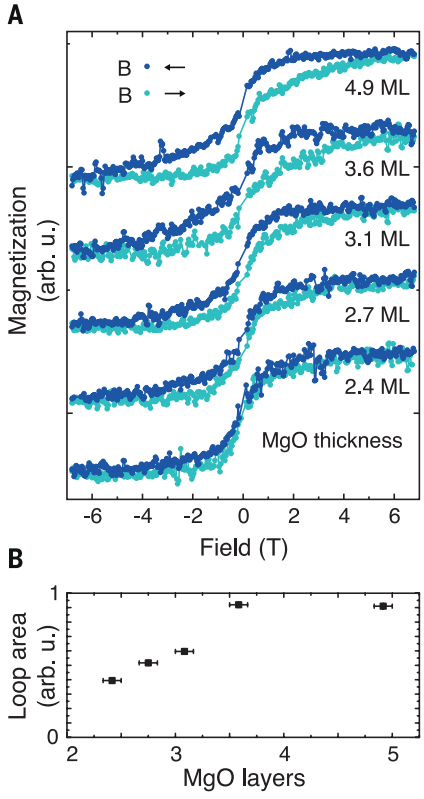

Fig. 4. Effect of the MgO layer thickness. (**A**) Magnetization loops acquired on Ho atoms on MgO films of various thicknesses as indicated close to each loop ($T = 2.5$ K, *dB/dt* = 12 mT/s, $\phi = 2.15 \times 10^{-2}$ nm^{-2} s^{-1}, $\Theta_{Ho} = 0.005$ to 0.010 ML). The curves were rescaled to the corresponding saturation value at $B = +6.8$ T. The reduced loop opening compared to that in Figs. 1 and 3 is a consequence of the higher photon flux and the lower sweep rate used here. (**B**) Loop area as a function of MgO thickness, reaching a constant value at 3.6 ML.

the MgO film was reduced below 3.6 monolayers (ML) and were almost closed for a thickness of 2.4 ML (Fig. 4). We observed essentially no variation in the XAS and XMCD spectra of Ho atoms with the number of MgO layers (fig. S5), hence the Ho ground state was unaffected by the MgO thickness. Thus, protection against first-order reversal is a necessary but not a sufficient condition to prevent magnetization reversal. To obtain long magnetic lifetimes in single atoms, an efficient decoupling from the electron and phonon bath is also required to ultimately suppress higher-order scattering processes that cannot be eliminated by symmetry. This result also suggests that long spin lifetimes are unlikely for single atoms in direct contact with a metal substrate.

The need of a decoupling layer to obtain long lifetimes is in stark contrast with the interpretation of STM experiments on Ho atoms on Pt(111), which reported telegraph noise in the differential conductance with characteristic times of up to 700 s at T = 0.7 K and zero field (*19*). This signal was interpreted as magnetic bistability and ascribed to a J_z = 8 ground state, as calculated by DFT, which would be protected by the C_{3v} symmetry of the adsorption site. However, XMCD measurements revealed that Ho atoms on Pt(111) have a ground state J_z = 6 that is incompatible with long spin lifetimes in a C_{3v}-symmetric crystal field (*27*). In addition, the magnetization curves at 2.5 K are fully reversible. According to these XMCD results, Ho/Pt(111) is a perfect paramagnet, as are all the other single atoms on surfaces previously reported. Moreover, subsequent STM experiments on the same system could reproduce neither telegraph noise nor spin excitations (*10*). Together with further STM observations on other 4f elements (*28*), this questions the interpretation of the results reported in (*19*) as magnetic bistability of Ho/Pt(111).

The relative simplicity of the Ho/MgO system, based on common physical deposition methods, as well as the planar geometry of the system opens the possibility of probing and manipulating the Ho spin and its environment in a controlled way. Using MgO as a decoupling layer could improve the magnetic stability not only of individual atoms but also of surface-supported molecular magnets, paving the road to scalable and robust nanoscale spintronic devices.

REFERENCES AND NOTES

1. R. Sessoli, D. Gatteschi, A. Caneschi, M. A. Novak, *Nature* **365**, 141–143 (1993).
2. N. Ishikawa, M. Sugita, T. Ishikawa, S. Y. Koshihara, Y. Kaizu, *J. Am. Chem. Soc.* **125**, 8694–8695 (2003).
3. M. Mannini *et al*., *Nature* **468**, 417–421 (2010).
4. J. M. Zadrozny *et al*., *Nat. Chem.* **5**, 577–581 (2013).
5. L. Ungur, J. J. Le Roy, I. Korobkov, M. Murugesu, L. F. Chibotaru, *Angew. Chem. Int. Ed.* **53**, 4413–4417 (2014).
6. J. D. Rinehart, M. Fang, W. J. Evans, J. R. Long, *J. Am. Chem. Soc.* **133**, 14236–14239 (2011).
7. S. Loth, S. Baumann, C. P. Lutz, D. M. Eigler, A. J. Heinrich, *Science* **335**, 196–199 (2012).
8. A. A. Khajetoorians *et al*., *Science* **339**, 55–59 (2013).
9. S. Yan, D.-J. Choi, J. A. J. Burgess, S. Rolf-Pissarczyk, S. Loth, *Nat. Nanotechnol.* **10**, 40–45 (2015).
10. M. Steinbrecher *et al*., *Nat. Commun.* **7**, 10454 (2016).
11. C. F. Hirjibehedin *et al*., *Science* **317**, 1199–1203 (2007).
12. F. Meier, L. Zhou, J. Wiebe, R. Wiesendanger, *Science* **320**, 82–86 (2008).
13. H. Brune, P. Gambardella, *Surf. Sci.* **603**, 1812–1830 (2009).
14. A. A. Khajetoorians *et al*., *Phys. Rev. Lett.* **106**, 037205 (2011).
15. F. Donati *et al*., *Phys. Rev. Lett.* **111**, 236801 (2013).
16. I. G. Rau *et al*., *Science* **344**, 988–992 (2014).
17. S. Baumann *et al*., *Science* **350**, 417–420 (2015).
18. P. Gambardella *et al*., *Science* **300**, 1130–1133 (2003).
19. T. Miyamachi *et al*., *Nature* **503**, 242–246 (2013).
20. C. Hübner, B. Baxevanis, A. A. Khajetoorians, D. Pfannkuche, *Phys. Rev. B* **90**, 155134 (2014).
21. P. Blaha, K. Schwarz, G. Madsen, D. Kvasnicka, J. Luitz, WIEN2k: An Augmented Plane Wave plus Local Orbitals Program for Calculating Crystal Properties (Karlheinz Schwarz, Techn. Universitat Wien, Austria, 2001).
22. Supplementary materials are available on *Science* Online.
23. M. Ganzhorn, S. Klyatskaya, M. Ruben, W. Wernsdorfer, *Nat. Nanotechnol.* **8**, 165–169 (2013).
24. J. Dreiser *et al*., *Appl. Phys. Lett.* **105**, 032411 (2014).
25. N. Ishikawa, M. Sugita, W. Wernsdorfer, *J. Am. Chem. Soc.* **127**, 3650–3651 (2005).
26. R. Giraud, W. Wernsdorfer, A. M. Tkachuk, D. Mailly, B. Barbara, *Phys. Rev. Lett.* **87**, 057203 (2001).
27. F. Donati *et al*., *Phys. Rev. Lett.* **113**, 237201 (2014).
28. D. Coffey *et al*., *Sci. Rep.* **5**, 13709 (2015).

ACKNOWLEDGMENTS

Funding from the Swiss National Science Foundation (grants 200021-153404, 200020-157081, 200021-146715, PZ00P2 142474, and IZ73Z0-152406) and the Swiss Competence Centre for Materials Science and Technology (CCMX) is gratefully acknowledged. L.P. was supported by an ETH Postdoctoral Fellowship (FEL-42 13-2). K.D. acknowledges support from the "EPFL Fellows" fellowship program cofunded by Marie Curie, FP7 grant agreement no. 291771. Z.S. was supported by the Serbian Ministry of Education and Science under grants ON171033 and ON171017. The DFT calculations were performed at the PARADOX-IV supercomputer at the Scientific Computing Laboratory (SCL) of the Institute of Physics Belgrade. The XMCD experiments were performed at the EPFL-PSI X-Treme beamline of the Swiss Light Source (SLS) and the ID32 beamline of the European Synchrotron Radiation Facility (ESRF). The authors declare that they have no competing financial interests.

SUPPLEMENTARY MATERIALS

www.sciencemag.org/content/352/6283/318/suppl/DC1
Materials and Methods
Figs. S1 to S9
Tables S1 to S3
References (*29*–*56*)

4 December 2015; accepted 8 March 2016
10.1126/science.aad9898

HYDROGEN BONDING

Nuclear quantum effects of hydrogen bonds probed by tip-enhanced inelastic electron tunneling

Jing Guo,[1]* Jing-Tao Lü,[2]* Yexin Feng,[1,3]* Ji Chen,[1] Jinbo Peng,[1] Zeren Lin,[1] Xiangzhi Meng,[1] Zhichang Wang,[1] Xin-Zheng Li,[4,5]† En-Ge Wang,[1,5]† Ying Jiang[1,5]†

We report the quantitative assessment of nuclear quantum effects on the strength of a single hydrogen bond formed at a water-salt interface, using tip-enhanced inelastic electron tunneling spectroscopy based on a scanning tunneling microscope. The inelastic scattering cross section was resonantly enhanced by "gating" the frontier orbitals of water via a chlorine-terminated tip, so the hydrogen-bonding strength can be determined with high accuracy from the red shift in the oxygen-hydrogen stretching frequency of water. Isotopic substitution experiments combined with quantum simulations reveal that the anharmonic quantum fluctuations of hydrogen nuclei weaken the weak hydrogen bonds and strengthen the relatively strong ones. However, this trend can be completely reversed when a hydrogen bond is strongly coupled to the polar atomic sites of the surface.

In terms of tunneling and zero-point motion, nuclear quantum effects (NQEs) play important roles in the structure, dynamics, and macroscopic properties of hydrogen-bonded (H-bonded) materials (*1*–*5*). Despite enormous theoretical efforts toward pursuing proper treatment of the nuclear motion at a quantum mechanical level (*5*–*9*), accurate and quantitative description of NQEs on the H-bonding interaction has proven to be experimentally challenging. Conventional methods for probing the NQEs are based on spectroscopic or diffraction techniques (*4*, *10*–*14*). However, those techniques have poor spatial resolution and only measure the average properties of many H bonds, which are susceptible to structural inhomogeneity and local environments. The spatial variation and interbond coupling of H bonds lead to spectral broadening that may easily smear out the subtle details of NQEs.

[1]International Center for Quantum Materials, School of Physics, Peking University, Beijing 100871, P. R. China. [2]School of Physics and Wuhan National High Magnetic Field Center, Huazhong University of Science and Technology, Wuhan 430074, P. R. China. [3]School of Physics and Electronics, Hunan University, Changsha 410082, P. R. China. [4]School of Physics, Peking University, Beijing 100871, P. R. China. [5]Collaborative Innovation Center of Quantum Matter, Beijing 100871, P. R. China.
*These authors contributed equally to this work. **†Corresponding author. E-mail: xzli@pku.edu.cn (X.-Z.L.); egwang@pku.edu.cn (E.-G.W.); yjiang@pku.edu.cn (Y.J.)**

Science
AAAS

Magnetic remanence in single atoms

F. Donati, S. Rusponi, S. Stepanow, C. Wäckerlin, A. Singha, L. Persichetti, R. Baltic, K. Diller, F. Patthey, E. Fernandes, J. Dreiser, Z. Sljivancanin, K. Kummer, C. Nistor, P. Gambardella and H. Brune (April 14, 2016)

Science **352** (6283), 318-321. [doi: 10.1126/science.aad9898]

Editor's Summary

Stable magnets from single atoms

An important goal in molecular magnetism is to create a permanent magnet from a single atom. Metal atoms adsorbed on surfaces can develop strong magnetization in an applied field (paramagnetism). Donati *et al.* show that single holmium atoms adsorbed on a magnesium oxide film grown on a silver substrate show residual magnetism for temperatures up to 30 K and bistabilty that lasts for 1500 s at 10 K (see the Perspective by Khajetoorians and Heinrich). The atom avoids spin relaxation by a combination of quantum-state symmetry and by the oxide film preventing the spin from interacting with the underlying metal via tunneling.

Science, this issue p. 318; see also p. 296

Science (print ISSN 0036-8075; online ISSN 1095-9203) is published weekly, except the last week in December, by the American Association for the Advancement of Science, 1200 New York Avenue NW, Washington, DC 20005.

www.sciencemag.org/content/352/6283/318/suppl/DC1

Supplementary Materials for

Magnetic remanence in single atoms

F. Donati, S. Rusponi, S. Stepanow, C. Wäckerlin, A. Singha, L. Persichetti, R. Baltic, K. Diller, F. Patthey, E. Fernandes, J. Dreiser, Ž. Šljivančanin, K. Kummer, C. Nistor, P. Gambardella,* H. Brune*

*Corresponding author. E-mail: pietro.gambardella@mat.ethz.ch (P.G.); harald.brune@epfl.ch (H.B.)

Published 15 April 2016, *Science* **352**, 318 (2016)
DOI: 10.1126/science.aad9898

This PDF file includes:

Contents

1 Sample Preparation

Low-temperature scanning tunneling microscopy (STM) and x-ray absorption spectroscopy (XAS) experiments were performed in three different experimental setups. In each of these ultra-high vacuum chambers, we prepared the Ag(100) single crystal in ultra high vacuum with repeated Ar^+ sputtering (ion energy of 1.2 keV) and annealing (800 K) cycles. MgO was grown by evaporation of Mg from a crucible in a O_2 pressure of 1×10^{-6} mbar with growth rates of $0.1 - 0.2$ monolayers (MLs) per minute at a sample temperature of 625 K. One MgO ML is defined as one Mg atom per substrate Ag atom. The MgO grows in a quasi layer-by-layer fashion (*29*). For XAS experiments, we prepared samples with more than 2.4 MgO layers to assure the required complete filling of the Ag surface. We calibrated the MgO coverage combining room temperature STM measurements with XAS spectra of the Mg K-edge for samples with close to half a monolayer of MgO. For thicker MgO films, we then estimated the number of MgO layers from the intensity of the Mg K-edge after MgO deposition. The low-temperature STM experiments were performed on samples with less than 1 ML MgO in order to preserve Ag areas for tip apex cleaning. To obtain large 2-ML-thick MgO islands on samples with less than 1 ML MgO coverage, we grew MgO keeping the sample at about 875 K, and the growth was followed by fast cooling to room temperature, as described in (*30*).

Samples of MgO/Ag(100) were transferred into the corresponding STM or XAS low temperature cryostat without breaking the vacuum. We deposited Ho atoms on the cold sample kept at temperatures ranging from 4 to 10 K in a pressure below 3×10^{-11} mbar. Similarly to what was done for the MgO calibration, the Ho coverage in XAS experiments was estimated comparing XAS and room-temperature STM measurements on reference samples covered by less than half a monolayer of Ho. Again, we define 1 Ho ML as one Ho atom per Ag substrate atom.

Since the XMCD studies had to be carried out on samples that showed no bare Ag(100), and since MgO does not grow layer-by-layer, the samples prepared for the XMCD experiments had a minimum MgO coverage of 2.4 ML. On 2 ML MgO, the Ho atoms have a narrow apparent height distribution (see Fig. S1) and are all located at identical adsorption sites (see Section 2). Conversely, Ho atoms on 1 ML MgO were found to adsorb on two different sites. Since the presence of two coexisting species can complicate the interpretation of ensemble measurements, we limit the XMCD investigation to samples with no or negligible amount of exposed first MgO layer, *i.e.* with a MgO thickness larger than 2.4 ML.

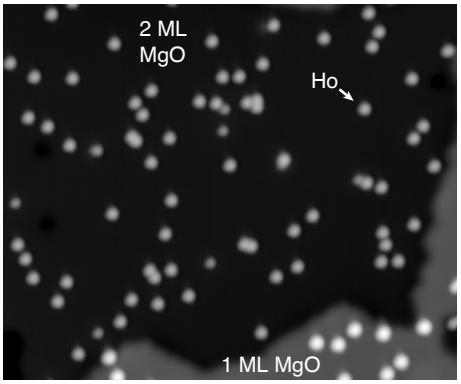

Fig. S1: **Ho atoms on** 2 **ML MgO/Ag(100).** STM image of 2 ML MgO/Ag(100) after the deposition of Ho atoms (sample bias $V_t = -100$ mV, tunnel current $I_t = 20$ pA, $T = 4.7$ K, Ho coverage $\Theta = 5.5 \pm 0.5 \times 10^{-}3$ ML). Size of the image: 39×32 nm^2. A small region of exposed 1 ML MgO is visible in the bottom right corner. At the used sample bias, the Ho atoms on the 2 ML MgO have an apparent height of 259 ± 6 pm. The elongated protrusions are two Ho monomers with an interatomic distance of at least 0.7 nm.

2 Measurements of the adsorption site of Ho atoms on MgO

According to our density functional theory (DFT) calculations (see Section 5), Ho atoms preferentially adsorb on top of an oxygen site. However, a direct experimental determination of the

adsorption site of Ho was not possible because the STM contrast of MgO depends on the tip apex, namely, from experiment to experiment once the Mg and once the O atoms were imaged as protrusions. In addition, the high conductance set-point required for atomically resolved images on MgO could not be used to image the Ho atoms because the tip displaced them. As an alternative method, we identified the adsorption site of Ho using co-deposited Co or Fe atoms as markers of the oxygen sites, on top of which they were predicted to adsorb (*16, 31–35*). We performed this measurement using the following procedure: first, on a sample spot without any adsorbed atoms, we acquired an atomically resolved image of the MgO surface, which allowed us to extract the spacing and the orientation of the MgO lattice (inset of Fig. S2). We obtained 292 ± 3 pm, which is in very good agreement with the values of the Ag(100) lattice spacing of 289 pm. This value also indicates that one of the two atoms (Mg or O) was measured as a protrusion, whereas the other appeared instead as a depression in the hollow position of the imaged lattice.

Second, using a lower conductance set-point, we acquired an STM image of a different surface spot in the presence of Co and Ho atoms without resolving the MgO lattice. To eliminate possible issues connected to piezoelectric creep which occurs after moving from spot to spot, the tip was left scanning on the same spot for at least one hour before recording the final STM image. At $V_t = -20$ mV and $I_t = 20$ pA (Fig. S2), Co atoms appear as protrusions with an apparent height of 139 ± 5 pm, in good agreement with the value reported in (*16*). Ho atoms appear with an apparent height of 218 ± 3 pm and, due to this increased apparent height and the tip convolution, they also appear wider. Both adatoms are thus easily distinguished by their different appearance. By extrapolating the MgO lattice extracted from the atomically resolved image onto the image with the adsorbates, we found that Co and Ho atoms adsorb on the same site (Fig. S2). Similar measurements performed using Fe atoms as markers gave identical results. Since first principle calculations found an O on-top adsorption for both Co, and

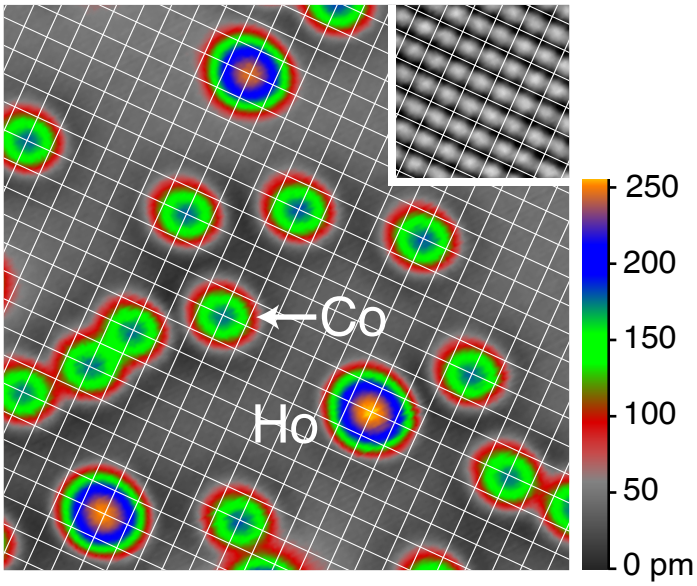

Fig. S2: **Adsorption site of Ho and Co atoms on** 2 **ML MgO/Ag(100).** STM image of 2 ML MgO/Ag(100) after the deposition of Co and Ho atoms ($V_t = -20$ mV, $I_t = 20$ pA, $T = 4.7$ K). Size of the image: 8.4×8.4 nm^2. **Inset**: atomically resolved STM image of the bare 2 ML MgO/Ag(100) surface ($V_t = -20$ mV, $I_t = 5.4$ nA, $T = 4.7$ K). The white grid extrapolates the MgO lattice onto the STM image with the adsorbates. Since the two images are acquired on different surface spots, the offset is a free parameter and has been chosen such that the grid matches the summit of the Co atom indicated by the white arrow.

Fe atoms, we infer that Ho, Co and Fe atoms all adsorb on top of O sites for MgO thicknesses of 2 ML.

3 Extended description of XAS and XMCD methods and results

X-ray absorption spectroscopy and magnetic circular dichroism (XCMD) measurements were performed in two different synchrotron facilities over five different measurement periods. Measurements shown in Fig. 1 were acquired at the ID32 beamline of the European Synchrotron Radiation Facility (ESRF), which is equipped with a cryostat with a base temperature of 3.5 K

and allowing magnetic fields of up to 9 T, with a maximum sweep rate of 50 mT/s. In this facility, we employed a defocussed beam with a spot size of 0.6×1.4 mm^2, allowing measurements with good signal-to-noise ratio with photon fluxes down to $\phi = 1 \times 10^{-2}$ nm^{-2}s^{-1}. All the other measurements shown in the present paper were acquired at the EPFL-PSI X-treme beamline at the Swiss Light Source (SLS), where the sample can be measured at a base temperature of 2.5 K in magnetic fields up to 7 T, with a maximum sweep rate of 33 mT/s (*36*). The maximum beam spot of 0.3×2 mm^2 allowed a good signal-to-noise ratio with photon fluxes down to $\phi = 0.55 \times 10^{-2}$ nm^{-2}s^{-1}. In both cases, the samples were measured in total electron yield (TEY) mode, which allowed the high sensitivity required by the extremely low concentrations of magnetic elements at the surface (*37*).

The XAS and XMCD spectra in saturation conditions (maximum field available and normal incidence) shown in Figs. 1D and S6 were obtained averaging over several (4 and 8, respectively) acquisitions of the I^+ and I^- absorption signals. The time required for a single spectrum ranges from 2 to 3 minutes. Prior to deposition of Ho, we recorded the background spectra on an MgO/Ag(100) substrate which was subtracted from the Ho XAS to eliminate any contribution from the substrate. Magnetization curves (Figs. 1, 3, 4 and S6) were obtained acquiring the I^+ and the I^- signal at the maximum of the M_5 edge at the energy of 1347.3 eV and dividing it by the corresponding pre-edge value acquired at 1340.3 eV. At the ESRF-ID32 beamline, the acquisition is performed in a step-by-step field ramp. The time required for ramping the field and acquiring the signal was about 30 s per point. The magnetization curve shown in Fig. 1E was measured by setting a field step of 0.2 T, corresponding to an average sweep rate of 8.3 mT/s. At the EPFL-SLS X-treme beamline, the magnetization curves were instead acquired by measuring the edge and pre-edge signals while ramping the field in an "on-the-fly" mode. This procedure allows faster field sweep rates of up to 33 mT/s. However, at the maximum available speed the noise level requires to average over multiple acquisitions to have a sufficient

signal-to-noise ratio, as done for the loops in Fig. 3. Therefore, for loops obtained in a single acquisition (Figs. 4A and S6D), we employed slower field sweep rates.

3.1 Magnetic lifetime measurements

The time-evolution of the XMCD signal at the magnetic field $B = 0.01$ T (Fig. 2C) was recorded with the following procedure: a) we ramped the magnetic field up $B = +6.8$ T; b) we waited several minutes for the magnetization to relax to saturation; c) we ramped down to $B = 0.01$ T with the maximum allowed speed of 33 mT/s; d) once the target field was reached, the maximum of the I^+ and I^- polarization at the M_5 edge, together with the corresponding pre-edge value, were alternatingly recorded as a function of time. The XMCD signal was obtained by dividing the edge (1347.3 eV) to the pre-edge (1340.3 eV) signals for each photon helicity. Our measurements showed a strong dependence of the magnetization lifetime on the photon flux (see below), as already reported for endofullerene single molecule magnets (*24*). Therefore, in order to best preserve the system close to saturation during the field sweep, the photon shutter was kept close while ramping down the field, and opened just before starting the XAS acquisition. In addition, we minimized the x-ray induced demagnetization by diluting the photon flux over a longer time period as described in (*24*). This was obtained by alternating acquisition periods (t_s), when the sample was exposed to the photon flux ϕ_s, and waiting periods with the beam shutter closed (t_w). This led to an effective photon flux $\phi = \phi_s t_s/(t_s + t_w)$. The curves in Fig. 2 of the main text were obtained with $t_s = 7$ s, $t_w = 21$ s, and $\phi_s = 0.55 \times 10^{-2}$ nm^{-2}s^{-1}, thus $\phi = \phi_s/4 = 0.14 \times 10^{-2}$ nm^{-2}s^{-1}.

Lifetime measurements to $B = +6.8$ T (Fig. 2D) were performed with a similar procedure. In this case, the Ho magnetization was first saturated at $B = -6.8$ T and the acquisition started after ramping the field at $B = +6.8$ T. The result of this procedure is shown in Fig. S3. Figure S3A displays the evolution of the Ho $\Delta\text{XAS}^{+(-)} = I^{+(-)}(t) - I^{+}(\infty)$ at $B = +6.8$ T,

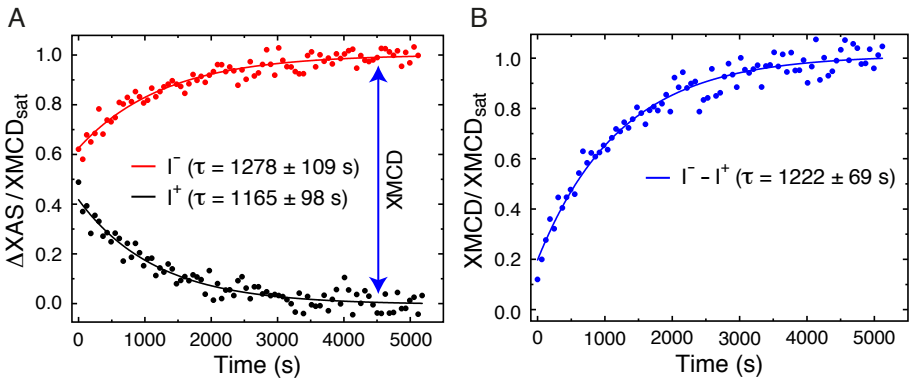

Fig. S3: **Details of lifetime measurements.** **A** Time-evolution of the I^+ and I^- signals. **B** Time-evolution of the XMCD. ($T = 10$ K, $B = 6.8$ T, MgO thickness $\Theta_{\mathrm{MgO}} = 6.0$ ML, Ho coverage $\Theta_{\mathrm{Ho}} = 0.015$ ML, $t_s = 7$ s, $t_w = 21$ s, $\phi_s = 0.55 \times 10^{-2}$ nm^{-2}s^{-1}, and $\phi = \phi_s/4 = 0.14 \times 10^{-2}$ nm^{-2}s^{-1}). Solid lines are fit to experiments (dots).

normalized to the asymptotic value of the $\mathrm{XMCD}_{\mathrm{sat}} = I^-(\infty) - I^+(\infty)$. The XMCD signal in Fig. S3B was obtained from the difference of the two helicity signals, and then normalized to $\mathrm{XMCD}_{\mathrm{sat}}$. The starting value of the normalized XMCD represents the magnetization of the system at the instant when the photon shutter was opened. Note that both the I^+ and the I^- signals show an exponential behavior with time, with opposite sign of the time-derivative. Independent fits of the two signals give identical values of τ within the error bars.

Measurements of the magnetic lifetime at 2.5 K (Fig. S4A) reveal an x-ray induced demagnetization, *i.e.*, the measurement influences the lifetime of magnetic quantum states of the Ho atoms, as also reported for endofullerene single molecule magnets (*24*). In that previous investigation, the rate of demagnetization was found to increase linearly with the photon flux and with the electron yield signal. Thus, the demagnetization process was attributed to the cascade of high-energy secondary electrons generated upon the absorption of the x-ray photons in the substrate. These electrons are in the conduction band of the substrate and lose their energy via scattering with defects, impurities, as well as with the adsorbed Ho atoms. Because of the large amount of energy they bear (up to a few eV), they can excite the magnetic atoms inducing tran-

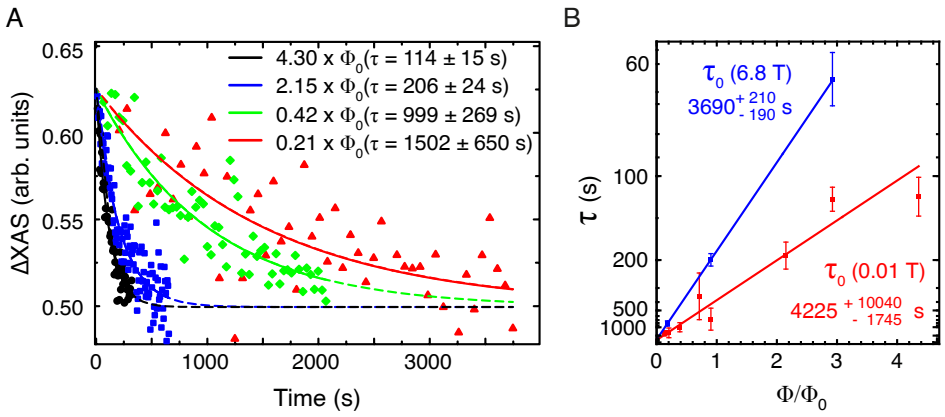

Fig. S4: **Flux-dependent magnetic lifetime at 2.5 K.** (**A**) Time evolution of the I^- ΔXAS intensity for different photon flux at $B = 0.01$ T, after saturation at $+6.8$ T. Since the decay rates of both circular polarizations are identical within the error bar, we limited the acquisition in many cases to the I^- signal. Full curves are exponential fits from which we extract the magnetization lifetimes. All curves are rescaled to match the initial and the asymptotic value of the red curve ($T = 2.5$ K, $\Theta_{\mathrm{Ho}} = 0.01$ ML, $\Theta_{\mathrm{MgO}} = 5.0$ ML, $\phi_0 = 1 \times 10^{-2}$ nm^{-2}s^{-1}, $\dot{B} = 33$ mT/s). (**B**) Magnetization lifetime as a function of the photon flux at 0.01 T (red) and 6.8 T (blue). Linear regressions yield the intrinsic lifetimes τ_0.

sitions to higher multiplets, from where the atoms decay to the lowest doublet, hence reducing their magnetic lifetime.

In order to estimate the intrinsic lifetimes of Ho atoms on MgO, we varied the incident photon flux ϕ. For a systematic investigation of τ as a function of the photon flux and magnetic field, the acquisition was limited to the I^- signal to reduce the acquisition time and, thus, possible effects due to sample degradation. The characteristic times for demagnetization (measured at $B = 0.01$ T after saturation at $B = +6.8$ T) and magnetization reversal (measured at $B = 6.8$ T after saturation at $B = -6.8$ T) are inversely proportional to ϕ (Fig. S4). Assuming photon-induced decay (τ_{ph}) and intrinsic relaxation (τ_0) to be two independent decay channels leads to $\tau^{-1} = \tau_0^{-1} + \tau_{\mathrm{ph}}^{-1}$. Our observations are perfectly reproduced by setting $\tau_{\mathrm{ph}}^{-1} = \sigma\phi$, where σ is the photon-induced demagnetization cross-section expressed in barn ($1\,\mathrm{b} = 10^{-24}$ cm^2).

For demagnetization at close to zero field, we find τ_0 of the order of one hour and $\sigma =$

2.4 Gb/atom. This is about 2 orders of magnitude larger than the cross-section for the photon absorption at the Ho M_5 edge (*38*), indicating that the photon-induced relaxation process is much more efficient than the direct x-ray absorption of the Ho atoms. This suggests that the atoms are demagnetized via secondary electrons created after the x-ray absorption in the substrate (*24*). Remarkably, at the largest accessible field, the intrinsic lifetime remains of the same order within the error bars (Fig. S4B). Such a weak dependence with the external field indicates that the first-order scattering with both Ag conduction electrons (*39*) and MgO phonons (*3*) is largely ineffective. Conversely, the photon cross-section for magnetization reversal $\sigma_{rev} = 5$ Gb/atom at $B = 6.8$ T is more than twice the value at close to zero field. This indicates that the scattering between the Ho atoms and the secondary hot electrons is more effective with a large magnetic field. Former experiments (*39*) and theoretical models (*40*) revealed that the scattering between magnetic atoms and electrons depends linearly on the Zeeman splitting of the lowest doublet. Therefore, a decreasing magnetic lifetime is expected with increasing Zeeman splitting of the quantum states. We speculate that a similar mechanism may enhance the scattering between the photon-induced hot electrons and Ho atoms at large magnetic fields, thus reducing the reversal time of Ho.

3.2 Influence of the MgO thickness on the magnetic properties of Ho atoms

Measurements of the XAS and XMCD of Ho atoms as a function of the MgO thickness show that the proximity to the silver substrate plays a negligible role in determining the magnetic ground state (Fig. S5). The spectral features of the M_5 edge remain essentially unchanged. The corresponding value of $\langle J_z \rangle$ extracted from the sum rules (*41, 42*) vary by less than 10% over the many measured samples, the remaining variations are mainly due to the inaccuracy of the background subtraction procedure. We conclude that the ground state of Ho atoms is

basically independent on the number of MgO layers, which justifies the comparison between STM measurements and DFT calculations, both performed for 2 ML MgO films, with XAS and XMCD data acquired on thicker MgO layers ($2.4 - 7$ ML).

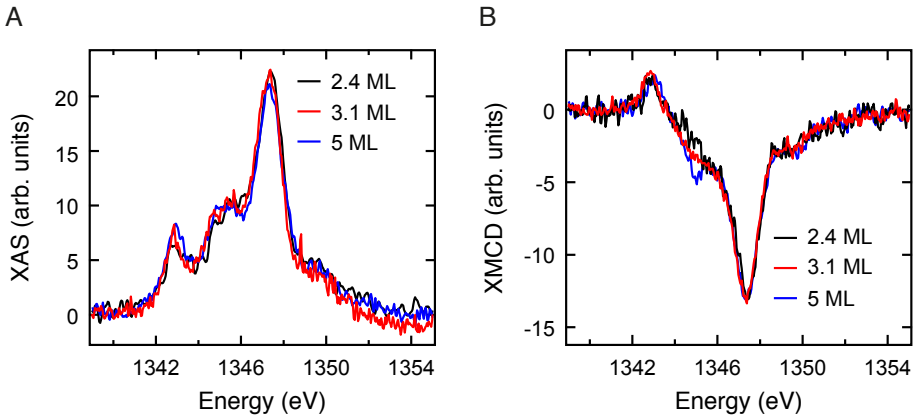

Fig. S5: **Influence of the MgO thickness.** (**A**) Normal incidence XAS ($I^+ + I^-$) of Ho atoms over the M_5 edge for samples with different thickness of the MgO film. (**B**) Corresponding XMCD spectra ($T = 2.5$ K, $B = 6.8$ T, $\phi = 2.15 \times 10^{-2}$ nm^{-2}s^{-1}). For all samples, the Ho coverage Θ_{Ho} ranges between 0.005 and 0.01 ML. In order to compare data of slightly different Ho coverages, spectra are normalized to the maximum of the XMCD.

4 Details of multiplet calculations

The XAS simulations are based on an atomic multiplet model that takes into account the electron-electron interaction among f- and d-electrons using rescaled Slater-Condon integrals, and the atomic spin-orbit interaction (*43–46*). The finite overlap of the rare-earth ion wave-functions with the surrounding atoms is neglected due to the well-screened character of the $4f$-states. The x-ray absorption spectrum for a polarization vector $\mathbf{e}_q$ is calculated based on Fermi's golden rule considering only allowed electric-dipole transitions,

$$W_{fi} \propto |\langle \Psi_f | \mathbf{e}_q \cdot r | \Psi_i \rangle|^2 \, \delta(E_f - E_i - \hbar\omega) \, . \tag{S1}$$

For the evaluation of the transition matrix elements the electric dipole operator for different polarizations and incidence angles is expressed by a linear combination of the spherical harmonics Y_1^0, Y_1^1, and Y_1^{-1} which correspond to the electric field parallel to z and the circular polarizations, respectively. The δ function assures energy conservation but will be replaced by a Lorentzian function to account for the finite lifetime of the core hole. The spectrum is further broadened by a Gaussian function to account for the experimental energy resolution. Due to the strong overlap of the core hole with the valence electron wavefunctions, the calculations must take into account the interaction between the hole and the valence levels. Hence, multiplet effects dominate the spectral shape. At finite temperature, the population of excited states of the initial state configuration is also taken into account by considering transitions from Boltzmann weighted initial states. The Hamiltonian of the initial and final states, *i.e.*, $3d^{10}\,4f^N$ and $3d^9\,4f^{N+1}$ for the $M-$edge, respectively, are diagonalized separately. The spectrum is then calculated from the sum of all possible transitions for an electron excited from the occupied $3d$ level into an unoccupied $4f$ level. In the crystal field limit, the ground state is given by a single electronic configuration f^N (where N is the number of valence f-electrons), split in energy by electron repulsion and a crystal field potential with a certain symmetry. The atomic Hamiltonian is given by

$$H = H_{\mathrm{atom}} + H_{\mathrm{cf}}\,, \tag{S2}$$

where

$$H_{\mathrm{atom}} = \sum_N \frac{p_i^2}{2m} + \sum_N \frac{-Ze^2}{r_i} + \sum_{\mathrm{pairs}} \frac{e^2}{r_{ij}} + \sum_N \zeta(r_i)\; l_i \cdot s_i\,, \tag{S3}$$

and

$$H_{\mathrm{cf}} = -e \sum_N V(\mathbf{r}_i)\,. \tag{S4}$$

This approach includes both electronic Coulomb interactions and spin-orbit coupling for each subshell. The first two terms of the atomic Hamiltonian H_{atom} give the average energy of

the configuration and contains the kinetic energy and the interaction of the electron with the nucleus. The third term is the electron-electron interactions term that results in the splitting of the electronic states into the well-known multiplets. The spherical part of the electron-electron repulsion can be separated and is added to the average energy. The remaining non-spherical part is treated explicitly. The last term in H_{atom} represents the spin-orbit interaction that is calculated for each shell and ζ is assumed to be constant within a shell. Thus, the non-spherical part of the electron-electron interaction and the spin-orbit interaction determine the relative energies of the different states within the atomic configuration. The electronic environment of the ion is taken into account by the crystal field Hamiltonian H_{cf},

$$V(r,\theta,\phi) = \sum_{n=0}^{\infty}\sum_{m=0}^{n} r^n \gamma_{nm} Z_{nm}(\theta,\phi)\,, \tag{S5}$$

where

$$\gamma_{nm} = \sum_{j=1}^{k} \frac{4\pi}{2n+1} q_j \frac{Z_{nm}(\theta_j,\phi_j)}{r_j^{n+1}}\,, \tag{S6}$$

and k is the number of coordinating atoms with charge q_j at positions (r_j,θ_j,ϕ_j). The $Z_{nm}(\theta,\phi)$ are the tesseral harmonics and the parameters γ_{nm} can be calculated from the positions and charges of the surrounding atoms. In general the potential function reflects the point symmetry of the lattice site. The less symmetric the site, the more terms occur in the expansion. It must be noted that the terms occurring depend on the axes chosen, and are in their simplest form when the axes are the symmetry axes of the point group. There are two general rules: firstly, if the lattice site posses inversion symmetry and/or mirror planes, then all odd-n terms vanish; secondly, if the z axis is an m-fold axis of symmetry, the potential will contain terms of Z_{nm}. For some high symmetry cases there exist relations between the coefficients of the tesseral harmonics of the same n. Nevertheless, not all the nonzero terms in the expansion of the potential will affect the energy levels of the ion, as their matrix elements may yet be zero. More specifically, for f-shell electrons only $n \leq 6$ terms yield non-zero matrix elements. Hence,

instead of calculating the non-zero γ_{nm} parameters, the prefactors $A_{nm} = \langle r^n \rangle \gamma_{nm}$ are treated as fit parameters in the calculations to match the experimental lineshape. In model Hamiltonians acting mostly only on the ground state multiplet, the crystal field potential is usually expressed in terms of the Stevens operators $\hat{O}^n_m$,

$$V_{\mathrm{cf}} = \sum_{n,m} B^n_m \, \hat{O}^n_m \, . \tag{S7}$$

Note, that there exist a direct relationship between the A_{nm} and B^n_m parameters that depends on the number of electrons in the considered shell. Thus the rules for non-vanishing γ_{nm} values apply also to the B^n_m parameters. The crystal field term is only applied to the outer shell, since the core hole in the excited state is well screened by the other electrons. In addition, the crystal field applied to the initial and final state is chosen to be the same, although the presence of the core hole and the Coulomb repulsion of the excited electron affects the radial extension of the wavefunction and hence the crystal field term. We neglect this effect in the XAS calculations. The spectral shape is mostly determined by the final state crystal field term and the nature of the ground state.

To calculate XAS spectra of magnetic ions and hence XMCD spectra, the Zeeman energy term,

$$H_{\mathrm{Z}} = \sum_{i=1}^{N} \frac{\mu_{\mathrm{B}}}{\hbar} \mathbf{B} \cdot (2\mathbf{s}^i + \mathbf{l}^i) \, , \tag{S8}$$

is added to the initial and final state Hamiltonian acting only on the valence shell. Here, $\mathbf{s}^i$ and $\mathbf{l}^i$ are the one-electron spin and orbital kinetic momentum operators that add up to give the total atomic spin ($\mathbf{S}$) and orbital moments ($\mathbf{L}$), respectively.

The many electron wavefunction of a single configuration is represented by a linear combination of determinantal product states with basis wavefunctions of the form $R_n(r) \, Y^k_m(\theta, \phi) \, \chi(\sigma)$, which separates into the radial part $R_n(r)$, the spherical harmonics Y^k_m for the angular dependence, and the spin function $\chi(\sigma)$. The matrix elements of the radial part for the different terms

of the Hamiltonian are expressed by the Slater-Condon-Shortley parameters (F_i and G_i). These values have been reduced to 73 percent of their Hartree-Fock calculated values to account for the overestimation of electron-electron repulsion in the free ion and for the delocalization and screening effects in the adatom system. The spin-orbit coupling constant ζ is obtained together with the F_i and G_i values using the atomic theory code developed by Cowan (*43*). The non-spherical part of the total Hamiltonian for the initial and final state is numerically diagonalized considering all contributions (electron-electron interaction, ligand field, spin-orbit coupling and magnetic field) simultaneously. This yields wavefunctions and energies from which we calculate also the expectation values of the spin and orbital moments. Our code is free of symmetry restrictions, *i.e.*, external fields can be applied in any possible direction.

The expectation values of the magnetic moments for the eigenstates can be directly calculated. The total moment of a shell is given by the operator

$$M = \sum_N m_i \,, \tag{S9}$$

where the m_i are the single electron spin or angular momentum operators. The same applies for the spin dipole operator. The expectation value of moment $\langle M_\theta^i \rangle$ of state i along the direction $\mathbf{e}_\theta$ is given by

$$\langle M_\theta^i \rangle = \langle \Psi_i | M_\theta \rangle \Psi_i = (\mathbf{e}_\theta \cdot \mathbf{e}_x) \langle M_x^i \rangle + (\mathbf{e}_\theta \cdot \mathbf{e}_y) \langle M_y^i \rangle + (\mathbf{e}_\theta \cdot \mathbf{e}_z) \langle M_z^i \rangle \,. \tag{S10}$$

To calculate the expectation value of the moment M at finite temperature, the states are weighted by the Boltzmann distribution according to

$$\langle M_\theta(T) \rangle = \frac{1}{Z} \sum_i \langle M_\theta^i \rangle \, e^{-\frac{E_i}{k_\mathrm{B} T}} \quad \text{with } Z = \sum_i e^{-\frac{E_i}{k_\mathrm{B} T}} \,. \tag{S11}$$

4.1 Ground state of Ho atoms on MgO

To gain insight in the magnetic moments and quantum states of Ho atoms, we simulated x-ray absorption spectra and equilibrium magnetization curves using multiplet calculations and com-

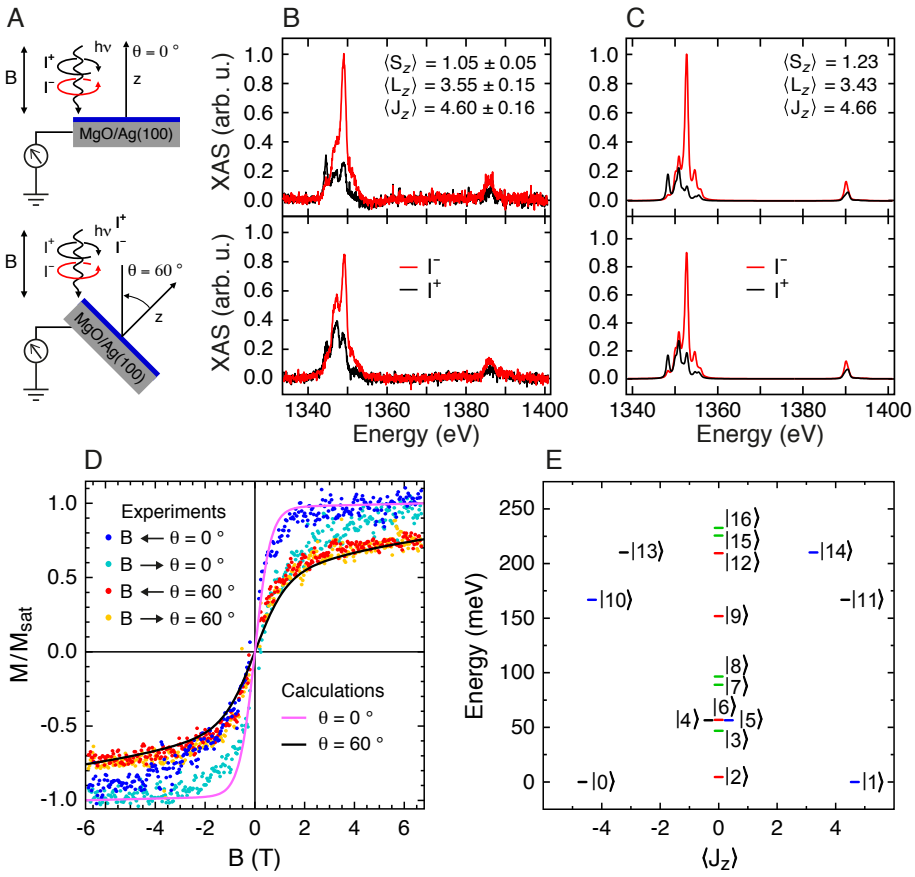

Fig. S6: **Comparison between experiment and multiplet calculations.** (**A**) Geometries of the XAS experiment for normal (top) an grazing (bottom) incidence. In both cases, the magnetic field is parallel to the photon beam. (**B**) Experimental and (**C**) calculated spectra for the two incident angles depicted in (**A**). Experimental conditions: $T = 2.5$ K, $B = 6.8$ T, $\phi = 2.15 \times 10^{-2}$ nm^{-2}s^{-1}, $\Theta_{\mathrm{Ho}} = 0.01$ ML, $\Theta_{\mathrm{MgO}} = 3.1$ ML. (**D**) Experimental hysteresis loops (dots, $\dot{B} = 12$ mT/s) and calculated equilibrium magnetization curves (solid lines) for the two incident angles. (**E**) Scheme of the quantum levels of the lowest $J = 8$ multiplet obtained from calculations (parameters of the calculation shown in Table S1). The color code identifies the states which are connected by symmetry operations within the C_{4v} group (*20*).

pared them with experimental data obtained at two different incidence angles θ (Fig. S6A to D). To obtain a meaningful comparison between equilibrium magnetization curves simulated by the multiplet analysis and experimental hysteresis loops, we employed a full data set acquired on a thin MgO layer (3.1 ML). On this sample, the hysteresis loop at grazing incidence is essentially

Table S1: Crystal field parameters used in multiplet calculations. Both A_{nm} and B_m^n coefficients are reported for completeness (see details in the previous section).

A_{20}	A_{40}	A_{44}	A_{60}	A_{64}
-30 meV	$+270$ meV	$+50$ meV	-410 meV	$+680$ meV
B_0^2	B_0^4	B_4^4	B_0^6	B_4^6
$+21.026$ μeV	-951.1 neV	-1.042 μeV	$+33.718$ neV	-443.876 neV

closed, hence it allows comparison with simulated equilibrium curves and, consequently, a precise assessment of the zero-field splitting. Since Ho atoms adsorb on the four-fold symmetric O site, only the crystal field operators allowed by the C_{4v} symmetry are included in the crystal field Hamiltonian:

$$H_{\rm cf} = e(B_0^2\,\hat{O}_0^2 + B_0^4\,\hat{O}_0^4 + B_4^4\,\hat{O}_4^4 + B_0^6\,\hat{O}_0^6 + B_4^6\,\hat{O}_4^6). \tag{S12}$$

The corresponding crystal field parameters, which were used as fitting parameters to reproduce the experiments, are summarized in Table S1.

Our multiplet calculations reveal a $4f^{10}$ occupation for the Ho atoms. This electronic configuration differs from that of the free atom ($4f^{11}$) and implies that, upon adsorption, one electron has been delocalized to the outer $6s6p5d$ orbitals, as also observed in previous XMCD investigations (*27*). Due to spin-orbit coupling, the lowest multiplet exhibits a total moment $J = 8$. The calculated splitting of these quantum levels is shown in Fig. S6E. Note that the XMCD spectral lineshape and magnetization curves depend on the character of the ground state and of the thermally populated excited states. Thus the accuracy of the level spacing in Fig. S6E is limited only to the lowest states. The Zeeman splitting of the lowest four levels, labelled from $|0\rangle$ to $|3\rangle$, is shown in Fig. 1C. At zero field, the ground state is a perfectly degenerate doublet with out-of-plane projections of the orbital $\langle L_z\rangle = 3.43$, spin $\langle S_z\rangle = 1.23$, and total moment $\langle J_z\rangle = 4.66$. These values are in very good agreement with those obtained by directly apply-

ing the sum rules (*41, 42*) to the experimental XAS and XMCD in saturation conditions, *i.e.*, at $T = 2.5$ K, $\theta = 0°$, and $B = 6.8$ T, for which we found $\langle L_z \rangle = 3.55 \pm 0.15$, $\langle S_z \rangle = 1.05 \pm 0.05$, and $\langle J_z \rangle = 4.60 \pm 0.16$.

The composition of the lowest Ho states in terms of the J_z states is given in Table S2. As the result of the four-fold ligand field of the O adsorption site, Ho levels are superpositions of pure J_z states separated by $\Delta J_z = 4$. The $|0\rangle$ and $|1\rangle$ states are composed of odd J_z states. As a consequence of their specific composition, direct transitions between $|0\rangle$ and $|1\rangle$ are only possible for scattering processes with $\Delta m = \pm 2$. Thus, the ground state doublet is protected from direct electron-induced transitions ($\Delta m = 0, \pm 1$). This remains valid at any external out-of-plane magnetic field since the J_z contributing to states $|0\rangle$ and $|1\rangle$ do not change (*20*). In addition, the phonon density of states vanishes for small energy splitting between the magnetic states, thus, in absence of an external magnetic field, direct scattering with phonons ($\Delta m = \pm 1 \pm 2$) (*3*) is absent. The system is further protected from direct phonon-induced transitions at finite fields by the limited density of low energy phonon modes in MgO, as discussed in Sec. 5.2. The absence of direct transitions allows for long magnetic relaxation times.

Multiplet calculations predict the first excited state, labelled as $|2\rangle$, to be a $\langle J_z \rangle = 0$ singlet lying 4.5 meV above the ground state (see Fig. 1C). This energy separation is sufficiently large to prevent level crossing of the lowest states up to more than 10 T, which explains the absence of steps in the hysteresis loop (*3*). In contrast to the $|0\rangle$, $|1\rangle$ doublet, the $|2\rangle$ state is a superposition of even J_z states. In this case, first-order electron- and phonon-induced excitations $|0\rangle \leftrightarrow |2\rangle$ and $|1\rangle \leftrightarrow |2\rangle$ are allowed, hence reversal of the magnetization is possible via excitation and subsequent de-excitation through the $|2\rangle$ state. However, this process requires a finite energy (4.5 meV in the absence of external field), therefore, it needs to be thermally activated or, alternatively, it can be triggered by the hot secondary electrons. We speculate that this reversal mechanism might be responsible of the reduced magnetic lifetime observed at 20 K (Fig. 2C)

Table S2: Composition of the lowest three magnetic states obtained from the multiplet calculations for zero magnetic field. The Ho states can almost entirely be described as a superposition of J_z states belonging to the lowest $J = 8$ multiplet. A remaining fraction (less than 2%), not included in the table, originates from mixing with higher multiplets $J = 7,\ 6$, etc.

J_z	$\|0\rangle$	$\|1\rangle$	$\|2\rangle$
-8	-	-	-
-7	57.1 %	-	-
-6	-	-	15.4 %
-5	-	0.6 %	-
-4	-	-	-
-3	26.5 %	-	-
-2	-	-	33.6 %
-1	-	14 %	-
+0	-	-	-
+1	14 %	-	-
+2	-	-	33.6 %
+3	-	26.5 %	-
+4	-	-	-
+5	0.6 %	-	-
+6	-	-	15.4 %
+7	-	57.1 %	-
+8	-	-	-

and at higher photon flux (Fig. S4). Other quantum levels lie from 45 to 230 meV higher in energy, therefore their effect on the magnetic properties of Ho atoms is not relevant at the temperatures and field employed in the present experiments.

5 Details of density functional theory calculations

The DFT calculations were performed using the Wien2k computer code (*21*) based on linearised augmented plane wave (LAPW) method (*47*). The atomic muffin-tin radii were set to 2.10 a.u., 1.74 a.u., 1.74 a.u., and 2.50 a.u., for Ho, O, Mg and Ag, respectively. For the LAPW basis functions in interstitial region we chose a planewave cut-off $K_{max} = 7/R_{mt}$, where R_{mt} is the

smallest atomic radius in the unit cell. The electronic exchange and correlations effects were described by the Perdew-Burke-Ernzerhof functional (PBE) (*48*) combined with the generalized gradient approximation (GGA) method including on-site Coulomb interactions U (*49*), in order to improve the description of the strong electron correlations in Ho $4f$ states. For the U parameter, we took the value of 5 eV (*19*). The Ag(100) surface was modeled with a three layer slab containing nine Ag atoms per fcc(100) layer. Atoms from the bottom Ag(100) layer are fixed in their bulk positions. Other Ag, Ho as well as O and Mg atoms from MgO layers deposited on top of Ag(100) were fully relaxed using the Newton algorithm. The k-point sampling of the Brillouin zones was done with 16 special Monkhorst-Pack points (*50*). The spin-orbit effects were described within a second variational method (*51, 52*). The adopted approach is one of the simplest and most reliable methods to calculate the electronic structure of systems with partially filled d or f bands. Alternative approaches based on hybrid functionals are less suitable because of the presence of the metal support.

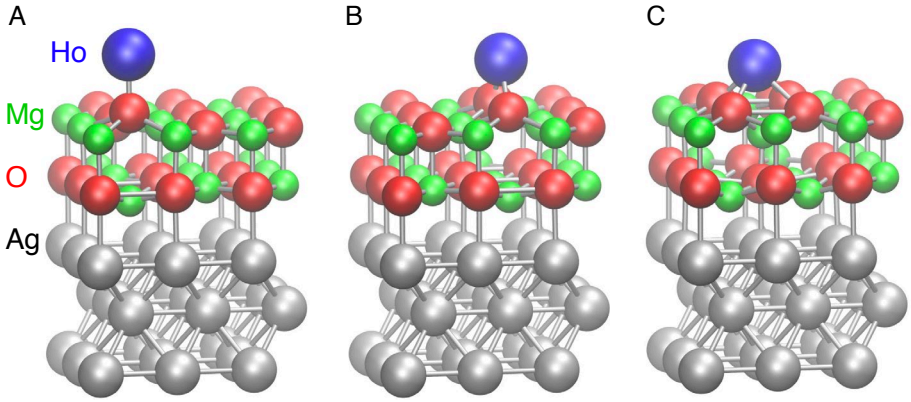

Fig. S7: **Calculated Ho adsorption sites on 2 ML MgO/Ag(100).** Ball-and-stick representation for the Ho adsorption on top of O (**A**), on the O-bridge site (**B**), and on top of Mg (**C**).

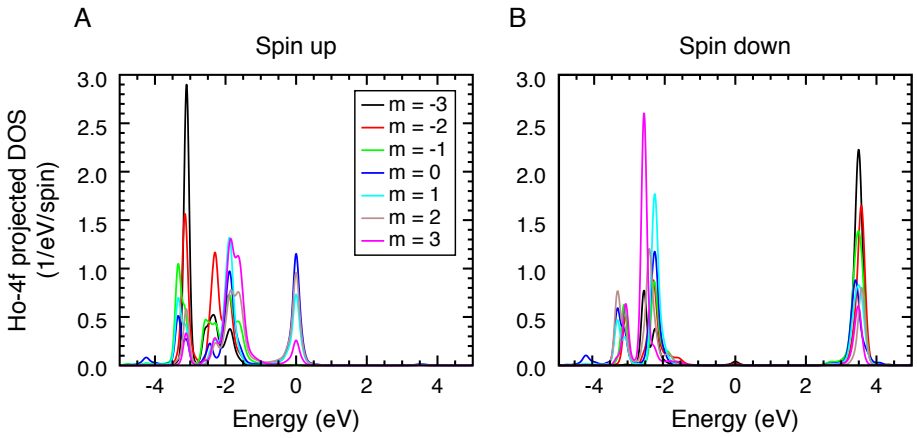

Fig. S8: **Density of states of a surface-adsorbed Ho atom.** (**A**) and (**B**) Spin-resolved $4f$-projected density of states of a Ho atom adsorbed on top of an O site on 2 ML MgO(100)/Ag(100) (see Fig. S7A).

Table S3: Total energies, spin and orbital magnetic moments, as well as Ho charge transfers for adsorption geometries presented in Fig. S7.

Adsorption site	Total energy (eV)	Spin mag. mom. (μ_B)	Orb. mag. mom. (μ_B)	Ho charge transfer (e)
O on-top	0.00	2.61	1.98	+ 0.12
O bridge	0.19	2.74	1.89	+ 0.71
Mg on-top	0.21	2.77	2.53	+ 1.21

5.1 Adsorption site and magnetic moments

In our DFT study we examined several adsorption sites of a Ho atom on 2 ML MgO(100) on a Ag(100) surface. Three stable sites found from our calculations are presented in Fig. S7. The corresponding energies, magnetic moments and charge transfer of the Ho atom are listed in Table S3. Total energies are given relative to the energy of the most favorable adsorption site (O on-top) depicted in Fig. S7A.

Our DFT calculations identify the O site as the most favorable one (Fig. S7A), whereas Ho adsorption on the bridge and the Mg sites are about 0.2 eV higher in energy. For the most

favorable O on-top adsorption, we find a weak charge transfer from the Ho to the surface O atom ($0.12\,e$). The specific $4f$ density of states of the Ho atoms on MgO (Figs. S8A and B) is quite different from that calculated for Ho on Pt(111) (*19*). In particular, the spin-up states are split over an energy range of about 4 eV, which is about two times higher than in the Pt(111) case. Since no hybridization is observed between the $4f$ states and the localized electrons of O and Mg, we ascribe the large splitting of Ho orbitals to a combined effect of the strong interaction between localized Ho $4f$ electrons and the electrostatic interaction induced by the close proximity with the underneath O atom. As a consequence of this large splitting, majority and minority $4f$ states partially overlap and the spin value is reduced to $\langle S_z \rangle = 1.1$. This value is in excellent agreement with those from sum rules and multiplet calculations and supports the identification of a ground state with reduced moment with respect to the free-atom ($|J_z| = 8$). The calculated orbital moment is, however, lower than the experimental value, in line with the general tendency of DFT to underestimate orbital moments in single atoms on MgO (*53*).

5.2 Calculations of the vibrational modes

The vibrational properties of a pristine 2 ML thin film of MgO on Ag(100) were calculated using the density functional perturbation theory approach (*54*) as implemented in Quantum Espresso (*55*). Cutoff energies of 40 and 400 Rydberg were employed for the plane wave expansion of electronic wave functions and for the electron density, respectively. The phonon densities of states (DOS) were calculated using a very dense 256×256 Monkhorst Pack mesh of q-vectors within surface Brillouin zone. Due to prohibitive computational cost of the *ab initio* study of the complete phonon spectra of the Ho/MgO/Ag(100) system, the Ho vibrational modes on MgO/Ag(100) were obtained applying the small displacement method where all atoms except the Ho and the underneath O are frozen at their equilibrium positions. Taking into account that the phonon modes of the Ag substrate are decoupled from those of the topmost

MgO layer (see below), the effect of Ag on the Ho vibrational modes was neglected.

The total and layer-projected phonon DOS of the bare 2 ML MgO/Ag(100) is shown in Fig. S9. Notably, our calculations indicate that a) in the low energy range the MgO phonon density is very low, thus MgO is a very efficient filter for the Ag phonons, and b) the MgO phonon density is extremely reduced in the energy range of interest defined by the zero-field splitting. These conclusions are in line with recent calculations on Fe/MgO/Fe tunneling junctions (*56*).

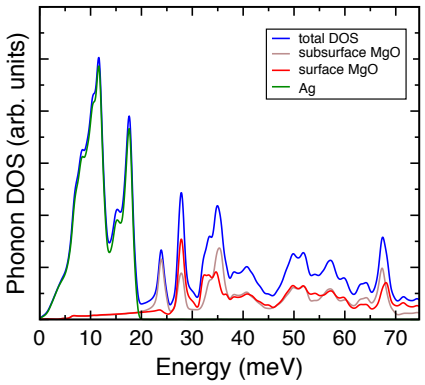

Fig. S9: **Density of phonon modes of a 2ML MgO/Ag(100) slab.** Phonon density of states projected onto the surface (blue) and subsurface (brown) MgO layer, as well as onto the Ag (black).

Calculations of the Ho on top of O on MgO/Ag(100), with only the Ho-O atoms unlocked from the equilibrium positions, reveal vibrational modes at the energies of 1.6, 4.3, and 8.5 meV. The first two modes involve the displacement of the Ho center in the xy plane, while the third is a stretching mode along the z-direction perpendicular to the surface. The first two in-plane modes can be effective in the exchange of angular momentum with the Ho atoms and potentially induce $\Delta m = \pm 1 \pm 2$ spin-excitations. Higher energy modes involve the motion of the O atom and lie above the range of energies accessible with the Zeeman splitting of the lowest doublet.

The presence of these discrete modes suggests two relevant points:

a) Although discretized, the vibrational modes of the Ho/MgO fall in the energy region of the Zeeman splitting of the lowest doublet. As this doublet is not protected against $\Delta m = \pm 2$ transitions, the hysteresis is expected to show steps at the specific fields at which the magnetization can relax by emission of a phonon. This is, however, in contrast with the experimental findings. A possible explanation is the extremely low density of phonons in the energy range of interest. Because of the high stiffness of the MgO, the number of available phonon modes at low energy is rather small, which intrinsically limits the possible coupling with the Ho-O vibrations. In addition, we can naively suppose that the in-plane Ho modes would preferentially couple with the optical modes of the MgO, which, in turn, are much higher in enery (more than 30 meV), hence providing another argument towards a weak coupling with the low-energy acoustic branch. As a consequence, Ho modes should be limitedly broadened and weakly effective in exchanging energy and momentum with the phonon bath.

b) The absence of modes at near-zero energy prevents the dissipation of the angular momenta of the Ho spin into the lattice. This is expected to seriously limit the effectiveness of the reversal of the magnetization even at low magnetic fields (less than about 0.2 T) where hyperfine level crossings are typically observed (*25, 26*). This might explain why the Ho/MgO seems so weakly perturbed by the crossing of the hyperfine levels around zero-field, in contrast to the $HoPc_2$ molecules (*25*).

6 References and Notes

1. R. Sessoli, D. Gatteschi, A. Caneschi, M. A. Novak, Magnetic bistability in a metal-ioncluster. *Nature* **365**, 141–143 (1993). doi:10.1038/365141a0

2. N. Ishikawa, M. Sugita, T. Ishikawa, S. Y. Koshihara, Y. Kaizu, Lanthanide double-decker complexes functioning as magnets at the single-molecular level. *J. Am. Chem. Soc.* **125**, 8694–8695 (2003). doi:10.1021/ja029629n Medline

3. M. Mannini, F. Pineider, C. Danieli, F. Totti, L. Sorace, P. Sainctavit, M.-A. Arrio, E. Otero, L. Joly, J. C. Cezar, A. Cornia, R. Sessoli, Quantum tunnelling of the magnetization in a monolayer of oriented single-molecule magnets. *Nature* **468**, 417–421 (2010). doi:10.1038/nature09478 Medline

4. J. M. Zadrozny, D. J. Xiao, M. Atanasov, G. J. Long, F. Grandjean, F. Neese, J. R. Long, Magnetic blocking in a linear iron(I) complex. *Nat. Chem.* **5**, 577–581 (2013). doi:10.1038/nchem.1630 Medline

5. L. Ungur, J. J. Le Roy, I. Korobkov, M. Murugesu, L. F. Chibotaru, Fine-tuning the local symmetry to attain record blocking temperature and magnetic remanence in a single-ion magnet. *Angew. Chem. Int. Ed.* **53**, 4413–4417 (2014). doi:10.1002/anie.201310451 Medline

6. J. D. Rinehart, M. Fang, W. J. Evans, J. R. Long, A $N3^{2-}$ radical-bridged terbium complex exhibiting magnetic hysteresis at 14 K. *J. Am. Chem. Soc.* **133**, 14236–14239 (2011). doi:10.1021/ja206286h Medline

7. S. Loth, S. Baumann, C. P. Lutz, D. M. Eigler, A. J. Heinrich, Bistability in atomic-scale antiferromagnets. *Science* **335**, 196–199 (2012). doi:10.1126/science.1214131 Medline

8. A. A. Khajetoorians, B. Baxevanis, C. Hübner, T. Schlenk, S. Krause, T. O. Wehling, S. Lounis, A. Lichtenstein, D. Pfannkuche, J. Wiebe, R. Wiesendanger, Current-driven spin dynamics of artificially constructed quantum magnets. *Science* **339**, 55–59 (2013). doi:10.1126/science.1228519 Medline

9. S. Yan, D.-J. Choi, J. A. J. Burgess, S. Rolf-Pissarczyk, S. Loth, Control of quantum magnets by atomic exchange bias. *Nat. Nanotechnol.* **10**, 40–45 (2015). doi:10.1038/nnano.2014.281 Medline

10. M. Steinbrecher, A. Sonntag, Mdos. S. Dias, M. Bouhassoune, S. Lounis, J. Wiebe, R. Wiesendanger, A. A. Khajetoorians, Absence of a spin-signature from a single Ho adatom as probed by spin-sensitive tunneling. *Nat. Commun.* **7**, 10454 (2016). doi:10.1038/ncomms10454 Medline

11. C. F. Hirjibehedin, C.-Y. Lin, A. F. Otte, M. Ternes, C. P. Lutz, B. A. Jones, A. J. Heinrich, Large magnetic anisotropy of a single atomic spin embedded in a surface molecular network. *Science* **317**, 1199–1203 (2007). doi:10.1126/science.1146110 Medline

12. F. Meier, L. Zhou, J. Wiebe, R. Wiesendanger, Revealing magnetic interactions from single-atom magnetization curves. *Science* **320**, 82–86 (2008).doi:10.1126/science.1154415 Medline

13. H. Brune, P. Gambardella, Magnetism of individual atoms adsorbed on surfaces. *Surf. Sci.* **603**, 1812–1830 (2009). doi:10.1016/j.susc.2008.11.055

14. A. A. Khajetoorians, S. Lounis, B. Chilian, A. T. Costa, L. Zhou, D. L. Mills, J. Wiebe, R. Wiesendanger, Itinerant nature of atom-magnetization excitation by tunneling electrons. *Phys. Rev. Lett.* **106**, 037205 (2011).doi:10.1103/PhysRevLett.106.037205 Medline

15. F. Donati, Q. Dubout, G. Autès, F. Patthey, F. Calleja, P. Gambardella, O. V. Yazyev, H. Brune, Magnetic moment and anisotropy of individual Co atoms on graphene. *Phys. Rev. Lett.* **111**, 236801 (2013).doi:10.1103/PhysRevLett.111.236801 Medline

16. I. G. Rau, S. Baumann, S. Rusponi, F. Donati, S. Stepanow, L. Gragnaniello, J. Dreiser, C. Piamonteze, F. Nolting, S. Gangopadhyay, O. R. Albertini, R. M. Macfarlane, C. P. Lutz, B. A. Jones, P. Gambardella, A. J. Heinrich, H. Brune, Reaching the magnetic anisotropy limit of a 3d metal atom. *Science* **344**, 988–992 (2014).doi:10.1126/science.1252841 Medline

17. S. Baumann, W. Paul, T. Choi, C. P. Lutz, A. Ardavan, A. J. Heinrich, Electron paramagnetic resonance of individual atoms on a surface. *Science* **350**, 417–420 (2015).doi:10.1126/science.aac8703 Medline

18. P. Gambardella, S. Rusponi, M. Veronese, S. S. Dhesi, C. Grazioli, A. Dallmeyer, I. Cabria, R. Zeller, P. H. Dederichs, K. Kern, C. Carbone, H. Brune, Giant magnetic anisotropy of single cobalt atoms and nanoparticles. *Science* **300**, 1130–1133 (2003).doi:10.1126/science.1082857 Medline

19. T. Miyamachi, T. Schuh, T. Märkl, C. Bresch, T. Balashov, A. Stöhr, C. Karlewski, S. André, M. Marthaler, M. Hoffmann, M. Geilhufe, S. Ostanin, W. Hergert, I. Mertig, G. Schön, A. Ernst, W. Wulfhekel, Stabilizing the magnetic moment of single holmium atoms by symmetry. *Nature* **503**, 242–246 (2013).doi:10.1038/nature12759 Medline

20. C. Hübner, B. Baxevanis, A. A. Khajetoorians, D. Pfannkuche, Symmetry effects on the spin switching of adatoms. *Phys. Rev. B* **90**, 155134 (2014). doi:10.1103/PhysRevB.90.155134

21. P. Blaha, K. Schwarz, G. Madsen, D. Kvasnicka, J. Luitz, WIEN2k: An Augmented Plane Wave plus Local Orbitals Program for Calculating Crystal Properties (Karlheinz Schwarz, Techn. Universitat Wien, Austria, 2001).

22. Supplementary materials are available on *Science* Online.

23. M. Ganzhorn, S. Klyatskaya, M. Ruben, W. Wernsdorfer, Strong spin-phonon coupling between a single-molecule magnet and a carbon nanotube nanoelectromechanical system. *Nat. Nanotechnol.* **8**, 165–169 (2013).doi:10.1038/nnano.2012.258 Medline

24. J. Dreiser, R. Westerström, C. Piamonteze, F. Nolting, S. Rusponi, H. Brune, S. Yang, A. Popov, L. Dunsch, T. Greber, X-ray induced demagnetization of single-molecule magnets. *Appl. Phys. Lett.* **105**, 032411 (2014). doi:10.1063/1.4891485

25. N. Ishikawa, M. Sugita, W. Wernsdorfer, Nuclear spin driven quantum tunneling of magnetization in a new lanthanide single-molecule magnet: Bis(phthalocyaninato)holmium anion. *J. Am. Chem. Soc.* **127**, 3650–3651 (2005).doi:10.1021/ja0428661 Medline

Formatted: Pattern: Clear

26. R. Giraud, W. Wernsdorfer, A. M. Tkachuk, D. Mailly, B. Barbara, Nuclear spin driven quantum relaxation in LiY0.998Ho0.002F4. *Phys. Rev. Lett.* **87**, 057203 (2001).doi:10.1103/PhysRevLett.87.057203 Medline

27. F. Donati, A. Singha, S. Stepanow, C. Wäckerlin, J. Dreiser, P. Gambardella, S. Rusponi, H. Brune, Magnetism of Ho and Er atoms on close-packed metal surfaces. *Phys. Rev. Lett.* **113**, 237201 (2014).doi:10.1103/PhysRevLett.113.237201 Medline

28. D. Coffey, J. L. Diez-Ferrer, D. Serrate, M. Ciria, C. de la Fuente, J. I. Arnaudas, Antiferromagnetic spin coupling between rare earth adatoms and iron islands probed by spin-polarized tunneling. *Sci. Rep.* **5**, 13709 (2015).doi:10.1038/srep13709 Medline

29. A. Ouvrard, J. Niebauer, A. Ghalgaoui, C. Barth, C. R. Henry, B. Bourguignon, Characterization of thin MgO films on Ag(001) by low-energy electron diffraction and scanning tunneling microscopy. *J. Phys. Chem. C* **115**, 8034–8041 (2011). doi:10.1021/jp1095823

30. J. Pal, M. Smerieri, E. Celasco, L. Savio, L. Vattuone, M. Rocca, Morphology of monolayer MgO films on Ag(100): Switching from corrugated islands to extended flat terraces. *Phys. Rev. Lett.* **112**, 126102 (2014).doi:10.1103/PhysRevLett.112.126102 Medline

31. A. Markovits, J. C. Paniagua, N. L'opez, C. Minot, F. Illas, Adsorption energy and spin state of first-row transition metals adsorbed on MgO(100). *Phys. Rev. B* **67**, 115417 (2003). doi:10.1103/PhysRevB.67.115417

32. K. M. Neyman, C. Inntam, V. Nasluzov, R. Kosarev, N. Rösch, Adsorption of *d*-metal atoms on the regular MgO(001) surface: Density functional study of cluster models embedded in an elastic polarizable environment. *Appl. Phys., A Mater. Sci. Process.* **78**, 823–828 (2004). doi:10.1007/s00339-003-2437-5

33. H. Y. T. Chen, G. Pacchioni, Properties of two-dimensional insulators: A DFT study of Co adsorption on NaCl and MgO ultrathin films. *Phys. Chem. Chem. Phys.* **16**, 21838–21845 (2014).doi:10.1039/C4CP03470H Medline

34. I. Yudanov, G. Pacchioni, K. Neyman, N. Rösch, Systematic density functional study of the adsorption of transition metal atoms on the MgO(001) Surface. *J. Phys. Chem. B* **101**, 2786–2792 (1997). doi:10.1021/jp962487x

35. Z. Šljivančanin, A. Pasquarello, Supported Fe nanoclusters: Evolution of magnetic properties with cluster size. *Phys. Rev. Lett.* **90**, 247202 (2003).doi:10.1103/PhysRevLett.90.247202 Medline

36. C. Piamonteze, U. Flechsig, S. Rusponi, J. Dreiser, J. Heidler, M. Schmidt, R. Wetter, M. Calvi, T. Schmidt, H. Pruchova, J. Krempasky, C. Quitmann, H. Brune, F. Nolting, X-Treme beamline at SLS: X-ray magnetic circular and linear dichroism at high field and low temperature. *J. Synchrotron. Radiat.* **19**, 661–674 (2012).doi:10.1107/S0909049512027847 Medline

37. P. Gambardella, S. S. Dhesi, S. Gardonio, C. Grazioli, P. Ohresser, C. Carbone, Localized magnetic states of Fe, Co, and Ni impurities on alkali metal films. *Phys. Rev. Lett.* **88**, 047202 (2002).doi:10.1103/PhysRevLett.88.047202 Medline

38. B. T. Thole, G. van der Laan, J. C. Fuggle, G. A. Sawatzky, R. C. Karnatak, J.-M. Esteva, 3*d* x-ray-absorption lines and the $3d^9 4f^{n+1}$ multiplets of the lanthanides. *Phys. Rev. B* **32**, 5107–5118 (1985).doi:10.1103/PhysRevB.32.5107 Medline

39. S. Loth, M. Etzkorn, C. P. Lutz, D. M. Eigler, A. J. Heinrich, Measurement of fast electron spin relaxation times with atomic resolution. *Science* **329**, 1628–1630 (2010).doi:10.1126/science.1191688 Medline

40. F. D. Novaes, N. Lorente, J.-P. Gauyacq, Quenching of magnetic excitations in single adsorbates at surfaces: Mn on CuN/Cu(100). *Phys. Rev. B* **82**, 155401 (2010). doi:10.1103/PhysRevB.82.155401

41. B. T. Thole, P. Carra, F. Sette, G. van der Laan, X-ray circular dichroism as a probe of orbital magnetization. *Phys. Rev. Lett.* **68**, 1943–1946 (1992). doi:10.1103/PhysRevLett.68.1943 Medline

42. P. Carra, B. T. Thole, M. Altarelli, X. Wang, X-ray circular dichroism and local magnetic fields. *Phys. Rev. Lett.* **70**, 694–697 (1993).doi:10.1103/PhysRevLett.70.694 Medline

43. R. D. Cowan, *The Theory of Atomic Structure and Spectra* (Univ. of California Press, Berkeley, 1981).

44. G. van der Laan, B. T. Thole, Strong magnetic x-ray dichroism in 2*p* absorption spectra of 3*d* transition-metal ions. *Phys. Rev. B* **43**, 13401–13411 (1991).doi:10.1103/PhysRevB.43.13401 Medline

45. F. de Groot, Multiplet effects in X-ray spectroscopy. *Coord. Chem. Rev.* **249**, 31–63 (2005). doi:10.1016/j.ccr.2004.03.018

46. F. de Groot, A. Kotani, *Core Level Spectroscopy of Solids* (CRC Press, Boca Raton, FL, 2008).

47. O. K. Andersen, Linear methods in band theory. *Phys. Rev. B* **12**, 3060–3083 (1975). doi:10.1103/PhysRevB.12.3060

48. J. P. Perdew, K. Burke, M. Ernzerhof, Generalized gradient approximation made simple. *Phys. Rev. Lett.* **77**, 3865–3868 (1996).doi:10.1103/PhysRevLett.77.3865 Medline

49. V. I. Anisimov, J. Zaanen, O. K. Andersen, Band theory and Mott insulators: Hubbard U instead of Stoner I. *Phys. Rev. B* **44**, 943–954 (1991).doi:10.1103/PhysRevB.44.943 Medline

50. H. J. Monkhorst, J. D. Pack, Special points for Brillouin-zone integrations. *Phys. Rev. B* **13**, 5188–5192 (1976). doi:10.1103/PhysRevB.13.5188

51. A. H. MacDonald, W. E. Picket, D. D. Koelling, A linearised relativistic augmented-planewave method utilising approximate pure spin basis functions. *J. Phys. C Solid State Phys.* **13**, 2675–2683 (1980). doi:10.1088/0022-3719/13/14/009

52. P. Novák, www.wien2k.at/reg_user/textbooks/novak_lecture_on_spinorbit.ps (1997).

53. S. Baumann, F. Donati, S. Stepanow, S. Rusponi, W. Paul, S. Gangopadhyay, I. G. Rau, G. E. Pacchioni, L. Gragnaniello, M. Pivetta, J. Dreiser, C. Piamonteze, C. P. Lutz, R. M. Macfarlane, B. A. Jones, P. Gambardella, A. J. Heinrich, H. Brune, Origin of

perpendicular magnetic anisotropy and large orbital moment in Fe atoms on MgO. *Phys. Rev. Lett.* **115**, 237202 (2015).doi:10.1103/PhysRevLett.115.237202 Medline

54. S. Baroni, S. de Gironcoli, A. Dal Corso, P. Giannozzi, Phonons and related crystal properties from density-functional perturbation theory. *Rev. Mod. Phys.* **73**, 515–562 (2001). doi:10.1103/RevModPhys.73.515

55. P. Giannozzi, S. Baroni, N. Bonini, M. Calandra, R. Car, C. Cavazzoni, D. Ceresoli, G. L. Chiarotti, M. Cococcioni, I. Dabo, A. Dal Corso, S. de Gironcoli, S. Fabris, G. Fratesi, R. Gebauer, U. Gerstmann, C. Gougoussis, A. Kokalj, M. Lazzeri, L. Martin-Samos, N. Marzari, F. Mauri, R. Mazzarello, S. Paolini, A. Pasquarello, L. Paulatto, C. Sbraccia, S. Scandolo, G. Sclauzero, A. P. Seitsonen, A. Smogunov, P. Umari, R. M. Wentzcovitch, QUANTUM ESPRESSO: A modular and open-source software project for quantum simulations of materials. *J. Phys. Condens. Matter* **21**, 395502 (2009).doi:10.1088/0953-8984/21/39/395502 Medline

56. J. Zhang, M. Bachman, M. Czerner, C. Heiliger, Thermal transport and nonequilibrium temperature drop across a magnetic tunnel junction. *Phys. Rev. Lett.* **115**, 037203 (2015).doi:10.1103/PhysRevLett.115.037203 Medline